

MANUFACTURING OF A GAS FOIL BEARING FOR PALM-SIZED  
TURBOMACHINERY

A Thesis

by

ANDRON JAYKONDOR CREARY

Submitted to the Office of Graduate Studies of  
Texas A&M University  
in partial fulfillment of the requirements for the degree of  
MASTER OF SCIENCE

May 2009

Major Subject: Mechanical Engineering

MANUFACTURING OF A GAS FOIL BEARING FOR PALM-SIZED  
TURBOMACHINERY

A Thesis

by

ANDRON JAYKONDOR CREARY

Submitted to the Office of Graduate Studies of  
Texas A&M University  
in partial fulfillment of the requirements for the degree of

MASTER OF SCIENCE

Approved by:

Chair of Committee,	Daejong Kim
Committee Members,	Hae-Kwon Jeong
	Hong Liang
Head of Department,	Dennis O'Neal

May 2009

Major Subject: Mechanical Engineering

## ABSTRACT

Manufacturing of a Gas Foil Bearing for Palm-Sized

Turbomachinery. (May 2009)

Andron Jaykondor Creary, B.S., Florida State University

Chair of Advisory Committee: Dr. Daejong Kim

Compliant Air Foil Bearings are used in a wide variety of applications. The versatility, ease of manufacture, and low cost of foil bearings are a few of the reasons foil bearing have been so thoroughly researched.

Miniaturization of gas foil bearings has been explored using silicon parts with marginal success. An approach utilizing a well known micro-fabrication technique called LIGA (German acronym meaning Lithography, Electroplating, and Molding) is suggested as an alternative method. X-ray LIGA and UV-LIGA were explored and elastic foundations 200 $\mu$ m and 1mm in depth were made for an impulse turbine test setup. The main difference in between the two methods is resolution and depth that each is capable of producing. In addition, precision machine forming was used to create a top foil for the foil bearing.

The predicted performance of the bearing was investigated through the orbit simulation method. A parametric study based on preload, as well as loss factor, was conducted in which the rotor speed was varied and the responses were used to create cascade plots. Both the response and cascade plots are useful to determine the onset of

instability and the maximum operating speed of the foil bearing manufactured through LIGA. The unique features of the gas foil bearing introduced provide great promise in terms of its application considering the high stable operating speed is just above 1000 krpm.

## DEDICATION

For my wife, Rumiko who inspires me to have a greater sense of dedication for all endeavors and to my parents and five brothers: Christopher, Darrio, Matthew, Stephen, and Obadiah, whose love and support has always been a great motivation.

## ACKNOWLEDGEMENTS

I would like to thank my committee chair, Dr. Daejong Kim for his support, friendship, and understanding. His guidance and technical input was most helpful and motivating. Thanks to my committee members, Dr. Hae-kwon Jeong and Dr. Hong Liang, for their guidance and support throughout the course of this research. Additionally, a special thanks to Dr. Hae-kwon Jeong who was kind enough to let me use his lab for many months toward the completion of the LIGA process. A special thanks is also extended to Dr. Jeong students, Inho Lee and Yeonshick Yoo, who both gave me great start-up advice on Lithography and the Scanning Electron Microscope. Further thanks to all the staff from the Microscopy and Imaging Center, Material Characterization Facility, and Turbo Lab who supported and assisted me socially and professionally.

Thanks also to my friends, colleagues, and the department faculty and staff for making my time at Texas A&M University a great experience. I also want to extend my gratitude to Dr. Karen Butler-Purry and Shannon Henderson at the TAMU Louis Stokes Alliances for Minority Participation (LSAMP) for their investment in time and mentorship. The LSAMP fellowship supported me for two years and it provided great opportunities and exciting venues to share research ideas. As a result, I developed a strong sense of the necessity for United States Citizens to promote the pursuit of advanced degrees and diversity in all science fields.

A special thanks to Aaron Rimpel who helped greatly with the test rig and many other technical aspects of this research. Additionally, I would like to thank Song Du who helped to setup the electroplating system. Also thanks to Eddy Denk, Phil, Brent, and all the machine shop staff at the Turbo Lab for their efforts to instruct and advise about proper machining practices. Thanks to Rohit Gargate who helped immensely with Scanning Electron Microscope sample preparation and magnification calibration.

Finally, thanks to my mother and father for their encouragement and to my wife for her patience and love.

## NOMENCLATURE

**Symbols**

C	Nominal clearance
$c_{eq}$	Equivalent damping of one half of a bump as show in fig. 9, a combination of the coulomb friction and squeeze film damping effect
$e_x$	Eccentricity in X direction
$e_y$	Eccentricity in Y direction
$F_{bX,Y}$	Dynamic bearing reaction forces
$F_{Di,j}$	Dynamic external forces acting on a single bump including the weight of the rotor and forces from the gas film
$F_{eX,Y}$	Sum of all the external forces applied to the bearing including the weight of the rotor and gas film
h	film thickness, $h(\theta, z) = C - r_g + (e_x + r_p) \cos \theta + e_y \sin \theta + w(\theta, z); \quad 0 < z < R / 2$ $h(\theta, z) = C - r_g + (e_x - r_p) \cos \theta + e_y \sin \theta + w(\theta, z); \quad R / 2 < z < R$
H	Non-dimensional thickness $H = \frac{h}{C}$
$k_{AB}$	Stiffness of one half of the arc beam
$k_{eq}$	Equivalent stiffness of one half of the arc, inner, and outer beam as show in fig. 9
$k_{IB}$	Stiffness of one half of the inner beam
$k_{OB}$	Stiffness of one half of the outer beam
L	Sub-bearing length
$m_r$	Mass of the rotor
p	pressure
P	Non-dimensional pressure $P = \frac{p}{p_a}$
$p_{4Di,j}$	Pressure at a node

$p_a$	Ambient pressure
$p_b$	Distance between foil bearing elastic supports, bump pitch
$R$	Bearing Radius
$r_p$	Preload offset distance
$t_b$	Thickness of top foil
$v_{Di,j}(\zeta)$	Local top foil due to sagging deflection only
$w_{Di,j}(\zeta)$	Local total top foil deflection at a node including sagging effects
$W(\theta,Z)$	Non-dimensional total top foil deflection including sagging effects, $W(\theta,Z) = \frac{w(\theta,z)}{C}$
$w(\theta,z)$	Total top foil deflection including sagging effects
$x$	Coordinate axis along the circumferential direction of the unwrapped bearing, $x = R \cdot \theta$
$X$	Global inertial coordinate
$Y$	Global inertial coordinate
$z$	Coordinate axis along the axial direction of the unwrapped bearing
$Z$	Non-dimensional axial coordinate of the unwrapped bearing, $Z = \frac{z}{R}$
$\alpha_f$	Sagging coefficient that applies sagging effect based on the thickness, length, and stiffness (EI) of the foil
$\Delta x$	Fixed coordinate difference between each node along the circumferential direction of the unwrapped bearing based on the number of nodes chosen between stiffness and damping elements
$\Delta z$	Fixed coordinate difference between each node along the axial direction of the unwrapped bearing based on the number of nodes chosen between stiffness and damping elements
$\gamma_b$	Structural loss factor

$\delta_{D_{i,j}}$	Deflection of the foil NOT including the sagging effects at each node
$\dot{\delta}_{D_{i,j}}$	Velocity of the foil NOT including the sagging effects at each node
$\varepsilon_X$	Non-dimensional eccentricity in X direction, $\varepsilon_x = \frac{e_x}{C}$
$\varepsilon_Y$	Non-dimensional eccentricity in Y direction, $\varepsilon_y = \frac{e_y}{C}$
$\zeta$	Local coordinate between nodes at each foil bump
$\theta$	Global inertial coordinate, $\theta = \frac{x}{R}$
$\Lambda$	Bearing number, $\Lambda = \frac{6\mu\omega}{p_a} \left( \frac{R}{C} \right)^2$
$\mu$	Air viscosity
$\tau$	Normalized time, $\tau = \omega t$
$\omega$	Speed of the journal

### Acronyms

AB	Partial arc beam
IB	Inner beam
OB	Outer beam
PMMA	Poly-methyl-meth-acrylate, a thermoplastic and transparent plastic with moderate properties
SEM	Scanning Electron Microscope
SU-8	Phenol-formaldehyde novolak resin, a highly functional polymeric epoxy resin
UV	Ultraviolet
LIGA	German acronym for Lithography, Electroplating and Molding

## TABLE OF CONTENTS

	Page
ABSTRACT .....	iii
DEDICATION .....	v
ACKNOWLEDGEMENTS .....	vi
NOMENCLATURE .....	viii
TABLE OF CONTENTS .....	xi
LIST OF FIGURES .....	xiii
LIST OF TABLES .....	xv
CHAPTER	
I INTRODUCTION .....	1
II LITERATURE REVIEW .....	4
Motivation .....	7
III RESEARCH OBJECTIVE .....	8
IV DESCRIPTION OF GAS FOIL BEARING .....	10
V MICROFABRICATION .....	16
UV-Lithography .....	16
Electroplating .....	21
Process Control: Current Density .....	25
Purification of Nickel Solution .....	27
VI CHALLENGES OF MICROFABRICATION .....	29
Photoresist Processing .....	29
Electroplating .....	31

CHAPTER	Page
VII TEST RIG DESIGN.....	32
Design Description.....	32
Design Requirements .....	33
VIII NUMERICAL SIMULATION .....	41
Model of Elastic Foundation .....	41
Model of the Hydrodynamic Pressure on the Top Foil.....	44
Orbit Simulation.....	50
Parametric Study .....	52
Simulation Results.....	54
IV CONCLUSION AND FUTURE WORK.....	61
REFERENCES.....	63
APPENDIX A .....	66
APPENDIX B .....	69
APPENDIX C .....	75
VITA .....	85

## LIST OF FIGURES

	Page
Figure 1 Illustration of Compliant Air Foil Bearing Working Principle.....	2
Figure 2 Elastic Foundation Layer for Mesoscale Foil Gas Bearings.....	10
Figure 3 Schematic of Conventional Macroscale Foil Gas Bearing [12]. ....	11
Figure 4 Assembly Scheme of Mesoscale Foil Gas Bearing. ....	13
Figure 5 Exaggerated Schematic of Elastic Foundation. ....	15
Figure 6 Photo of X-ray Mask.....	20
Figure 7 SEM Image. ....	21
Figure 8 Electroplating [18]. ....	23
Figure 9 Test Rig and Experimental Setup.. ....	33
Figure 10 Test Rig, General Layout of Components. ....	34
Figure 11 Turbine and Turbine Shroud Dimensions (units: inches).....	35
Figure 12 Base Plate and Bearing Housing Dimensions (units: inches).....	36
Figure 13 Thrust Bearings Dimensions (units: inches).....	37
Figure 14 Sensor Holder Parts (units: inches).....	38
Figure 15 Components of the Test Rig .....	40
Figure 16 Elastic Foundation Schematic.....	43
Figure 17 Coordinate Systems for Analyses. ....	45
Figure 18 Exaggerated Description of Top Foil Sagging .....	47
Figure 19 Index for Nodal Pressures.....	48
Figure 20 Cascade Plot X , 50-350krpm, PL12um, LF0.20.....	56

	Page
Figure 21 Cascade Plot X, 50-500krpm, PL 17um, LF 0.20.....	57
Figure 22 Cascade Plot X, 50-500krpm, PL22um, LF 0.20.....	58
Figure 23 Cascade Plot X, 50-500krpm, PL17um, LF 0.15.....	59
Figure 24 Cascade Plot X, 50-500krpm, PL17um, LF 0.25.....	60
Figure 25 Fiber Optic Sensor 2618. ....	70
Figure 26 Fiber Optic Sensor 2618: First Linear Region.....	71
Figure 27 Fiber Optic Sensor 2618: Second Linear Region. ....	71
Figure 28 Fiber Optic Sensor 2619. ....	73
Figure 29 Fiber Optic Sensor 2619: First Linear Region.....	73
Figure 30 Fiber Optic Sensor 2618: Second Linear Region. ....	74
Figure 31 SU-8 Pattern.....	76
Figure 32 Detail of the SU-8 Pattern.....	77
Figure 33 Multiple Electroplated Elastic Foundations for Foil Bearing.....	78
Figure 34 Single Electroplated Elastic Foundation for Foil Bearing.....	79
Figure 35 Detail of the Single Electroplated Elastic Foundation.....	80
Figure 36 Electroplated Elastic Foundation for Foil Bearing.. ....	81
Figure 37 Detail of the Electroplated Elastic Foundation for Foil Bearing. ....	82

## LIST OF TABLES

	Page
Table 1 Chemical Quantities for Nickel Electroplating.....	25
Table 2 Geometry and Parameters for the Simulated Air Foil Bearing.....	53
Table 3 Original Data from UV-Lithography. ....	66
Table 4 Initial Conditions Data Fiber Optic Sensor (FOS) 2618.....	69
Table 5 Original Measurement Data Fiber Optic Sensor (FOS) 2618.....	69
Table 6 Initial Conditions Data Fiber Optic Sensor (FOS) 2619.....	72
Table 7 Original Measurement Data Fiber Optic Sensor (FOS) 2619.....	72

## CHAPTER I

### INTRODUCTION

Compliant Air Foil Bearings (CAFBs) are used in a wide variety of applications from cryogenic turbo-pumps to high temperature Auxiliary Power Units (APUs) for military vehicles. Foil bearings have many advantages and are more desirable due to higher efficiency, reduced noise pollution, and lower maintenance costs than oil-lubricated bearings [1]. Foil Bearings are especially useful for applications of continuous high speed operation, moderate loads, and high temperature [2]. Due to recent advancements foil bearings are becoming increasingly useful for high load applications.

The CAFBs consist of five main features as shown in Figure 1 the bearing housing, foil structure, smooth top foil, air film, and journal (the part of a shaft that passes through the bearing). The main principle of foil bearings is the hydrodynamic action or convergent pressure difference that allows the journal to be airborne on a thin film of gas during operation. As a journal spins, gas i.e. air is forced around the shaft. With careful design, a stable pressure field can be achieved around the shaft inducing an upwardly force that keeps the shaft away from the stationary part of the bearing, while reducing whirl phenomenon for many operating conditions. This state of operation is nearly frictionless since the main source of friction is from the interactions between the top foil, rotor and gas film.

---

This thesis follows the style of ASME Journal of Tribology.

Whirl phenomenon is a circular whipping motion of the shaft caused by imbalances and eccentricities in the shaft and mountings. This type of motion occurs in every shaft to some degree since no shaft can be perfectly balanced or aligned.

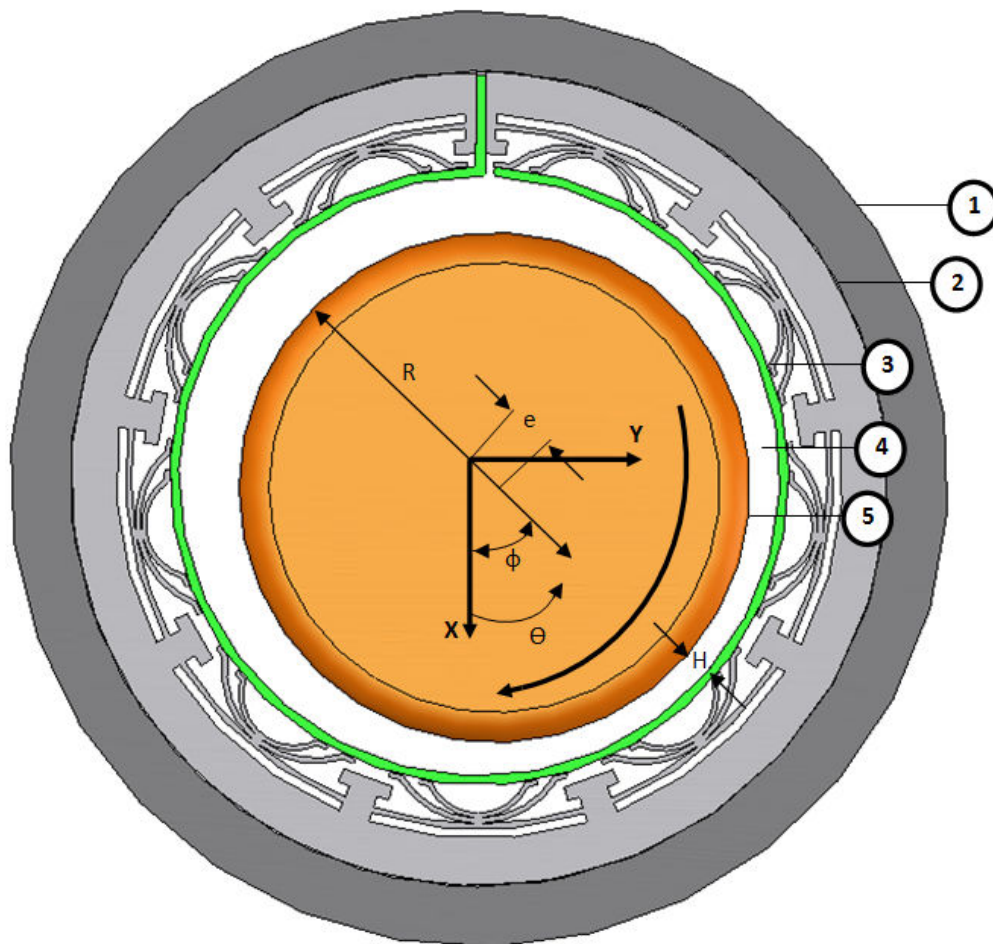


**Figure 1 Illustration of Compliant Air Foil Bearing Working Principle. (1) Bearing Housing, (2) Elastic Foundation of Foil Bearing, (3) Top Foil, (4) Air Film and (5) Journal. Where the Thickness Is Given By  $H=c - e \cos(\theta - \phi)$ .**

One of the main challenges for designing foil bearing is the stiffness and damping characteristics which are the key features that allows the foil bearing to possess many of its functional characteristics. The stiffness is determined by the geometry of bearing and the elastic foundation's material properties, position of journal center with respect to the bearing center as well as spin rate, while the damping is caused by a combination of the gas film squeeze and top foil slipping effect (coulomb friction) which are also dependent on spin rate, pressure field, and many other factors.

Due to the interdependence of variables and the iterative nature of designing foil bearings it is not possible to control every single aspect, but designers must consider all these effects. Designing a bearing that will stabilize a spinning rotor that has eccentricities and misalignment is a daunting task but due to the unique nature of compliant foil bearings all of these issues can be compensated for to a great degree. The focus of designer is often around the task of providing the compliance for shaft growth that occurs, due to centrifugal forces at high operating speeds, as well as stiffness and damping characteristics that promote stability. Considering the focus on compliance and the necessity for stability of the shaft motion, the bearing's material properties are of great importance for making an effective design.

## CHAPTER II

### LITERATURE REVIEW

Research on foil bearing has been focused on the macro-scale for many years. One useful summary outlining the recent state of CAFBs from the early 1970's to the late 1990's was written by Agrawal [3], the developer of the second generation CAFBs, his summary provides details of the major developments for air foil bearings. Agrawal describes the general working principle of foil bearings and states the major advantages of CAFBs noting that they have higher reliability, no scheduled maintenance, soft failure, and environmentally durable. He also mentions several companies that pioneered research for foil bearings as well as the many applications of CAFBs. Agrawal implies that foil bearings have a broader applicability than Air Cycle Machines which is widely used in Environmental Control Units onboard aircrafts and one of the primary applications for CAFBs at that time.

Heshmat [2] is one of the first authors to analyze the air foil bearings in detail and determine the pressure profile from the Reynolds equation using a numerical simulation. He also evaluated the effects of different operating conditions and parameters like speed, clearance and load on bearing performance.

Heshmat et al [4] presents a theoretical model of a bump type gas foil bearings and explores the relationships between the load, deflection, stiffness, and damping. Friction forces are accounted for in the modeling along with localized force interaction,

bump geometry, and variability of load distribution. The friction forces are considered between the bump foils and top foil as well as the bump foils and the bearing housing.

A companion to the previous reference, presents experimental verification by Heshmat et al [5] published in the same year. The experimenters used an optical measurement system while loading the air foil bearings in a variety of conditions. For linear regions of loading the authors were able to match results to their theoretical simulations. The paper offers good resources to designers who would like to see the limits of compliant air foil bearing and the empirical relations given are useful to enhance understanding and designs.

Using a finite element approach Peng and Carpino [6] create a structural model of a top foil and calculate the stiffness and damping coefficients for an elastically supported foil bearing. For simplicity inertial effects of the foil were neglected as well as bending of the membrane. Using the Reynolds equation and finite element approach they calculated the pressure profile and film thickness. A key observation reported shows that at high speeds the stiffness is dominated by the underlying elastic foundation while at low speeds the stiffness is heavily dependent on hydrodynamic gas film.

Heshmat [7] reports both speed and load performance achieving 2200 cps (132,000 rpm) and a load capacity of 727.8 N (163.6 lb) corresponding to a projected area pressure of 673.5kPa (97.68 psi) at an operating speed of 995 cps (59,700 rpm). Pushing foil bearings to a new level, Heshmat notes that during the testing the bearings demonstrated a strong stabilizing characteristic which he attributed to the findings from his data that confirm an increasing trend in stiffness of the foil bearing as the load

increases. The maximum displacement of the shaft in his experiment is about 1 mil, half of the 2 mil maximum allowable value designated by the American Petroleum Institute (API) standard for the peak to peak amplitude of unfiltered vibration. Heshmat also analyzes the magnitude of the displacement with respect to frequency or bode plot used for the identification of resonance speeds of the system. At lower frequency the maximum displacement is well below the API standardized limits and at the operating speed the vibration is almost negligible at 20  $\mu\text{m}$  (0.79 mils). The author implies that CAFBs have even greater potential in speed and load bearing capability than what he has done. Heshmat states that in terms of speed, the main limiting factor was not a result of the bearing characteristics but more so due to the limit of the air driven impulse turbine and speed of sound.

Han et al [8] determined the force coefficient using the perturbation method of analysis and the characteristics of air bearings with external pressurization. This study involved an analytical orbit simulation that was experimentally verified. The main purpose was to determine the parameters that affected the bearing coefficients i.e. external pressure, supply governors and the size of the bearing were all investigated for their effects.

Many different parameters are important for an effective design of a CAFB. Researchers have explored and understood numerous aspects of the foil bearing. However, unexplored territory of CAFBs includes the miniaturization of this reliable and versatile device.

**Motivation**

Increasing the load capabilities and stable operating speeds of foil bearings are important for expanding its applications, but research in miniaturization of the foil bearing has the potential of broadening the whole field of Turbomachinery. Mesoscale fuel based power generation has the potential to challenge batteries in terms of power density. The inherent challenge for Mesoscale Turbomachinery is the effects of downscaling. Vleugels [9] investigates at the top level some of the challenges for creating micro-gas turbines. According to Vleugels, a compressor that is made at the mesoscale needs to operate upwards of 500,000 rpm in order to obtain a reasonable efficiency. The operating speed alone limits the choice of bearings, but another concern is the temperature at which the bearings must operate. Parts that are near the side of a turbine can reach as much as 1000°C. Due to these two contributing factors Vleugels suggest that only CAFBs are capable of meeting such harsh operating conditions.

### CHAPTER III

#### RESEARCH OBJECTIVE

Fabricating a metallic mesoscale bearing poses a significant challenge. A common approach involves micromachining or precision machining since very small devices have parts or features on the order of microns. The main issue with utilizing micromachining is that the geometries are limited just as in macroscale machining. However, microfabrication techniques have no such issue.

In order to utilize a microfabrication, e.g. LIGA the proper processing conditions must be obtained. The proposed method is to create an approximately 200  $\mu\text{m}$  thick multi-bearing electroplating mold from phenol-formaldehyde novolac resin (SU-8) photoresist utilizing photoresist manufacturer guidelines as well as a pre-existing bearing design and optical mask made by Dr. Daejong Kim. Find the appropriate electroplating conditions and use the aforementioned multi-bearing foundation mold to create several bearing elastic foundations approximately 200 $\mu\text{m}$  in length. The next component requires the creation of a top foil hot forming jig to make precision top foils for the bearing. Using the 200 $\mu\text{m}$  elastic foundation and top foil assemble the bearing in the bearing housing for a test setup.

Design and create a testing apparatus to assess the fitness of the bearings by utilizing a simple impulse turbine test setup. The test rig should include a base plate that grounds the bearing housing, thrust bearings, turbine and turbine shroud. In addition, the

testing apparatus should be capable of measuring the unfiltered and filtered peak to peak vibration, the frequency of rotation, and time.

Finally for design improvements, an orbit simulation developed by Dr. Daejong Kim assessed the fitness of the bearings made using LIGA. Using the gathered simulation data, analysis should be conducted including but not limited to orbit plots, Fast Fourier Transform, and maximum stable operating speed.

## CHAPTER IV

### DESCRIPTION OF GAS FOIL BEARING

Lithographically manufactured mesoscale foil gas bearings have unique features that precision-machined foil bearings [10, 11] cannot provide. Figure 2 shows the design of elastic foundation used in this work. Unlike bump foils with a continuous corrugated foundation shown in Figure 3, the lithography manufactured elastic foundation is comprised of multiple independent bump sets. Each bump set consists of inner bump (IB), outer bump (OB), and a partial arc beam (AB).

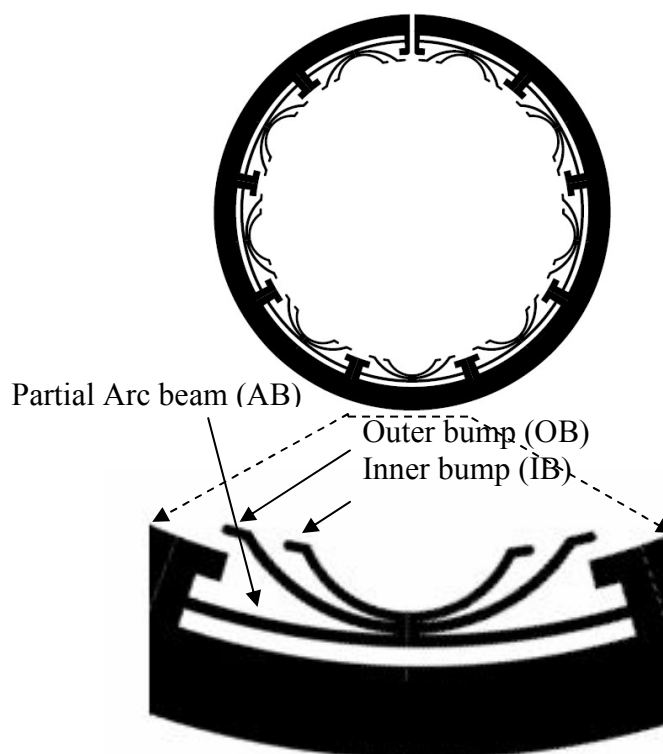


**Figure 2 Elastic Foundation Layer for Mesoscale Foil Gas Bearings.**

A unique feature of mesoscale foil gas bearings that can be manufactured through the LIGA method developed are various compliant wall structures that cannot be made via traditional precision machining or silicon micromachining. For example, each bump set in Figure 2 provides independent stiffness and damping to the top foil unlike macro scale foil bearings in Figure 3, where bump foils are continuous and it is difficult to analyze the overall characteristics. Each bump can be engineered and designed differently along the circumferential direction for improved bearing performance. The IB and OB provide parallel stiffness combined with the AB in a series to the IB and OB. Stiffness of these spring elements can be calculated using elementary beam theory.

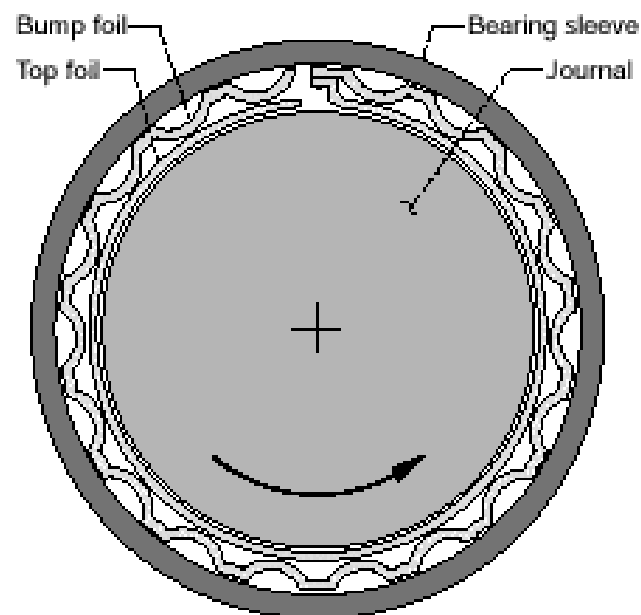


**Figure 3 Schematic of Conventional Macroscale Foil Gas Bearing [12].**

Figure 4 shows overall assembly procedure of mesoscale foil gas bearing. The multiple elastic foundation layers are assembled into the top foil (made of very thin sheet metals via hot forming) through the grooves on the elastic foundation layers which are formed as an integral part of the lithography process. A precision-machined split-type bearing sleeve encloses the top foil-elastic foundation assembly to complete the bearing. Because each elastic foundation layer provides independent support to the top foil along the axial direction, they do not have to be bonded together. This adds another benefit and advantage to the proposed design/manufacturing approach over the traditional precision machining; each elastic foundation layer can be engineered and manufactured independently with different stiffness and damping along the bearing length.

Parametric studies on macroscale foil bearings [13] indicate that foil gas bearings with three top foil pads with non-circular geometry have superior rotordynamic performance as compared to bearings with a continuous cylindrical top foil. In macroscale foil gas bearings, the bearing sleeve can be machined with certain geometry such that the final bearing surface on the top foil follows non-circular geometry. However, with mesoscale foil gas bearings, the non-circular bearing geometries cannot be achieved easily using traditional precision machining. Adopting lithography techniques for the elastic foundations can overcome this kind of problem without any difficulty.

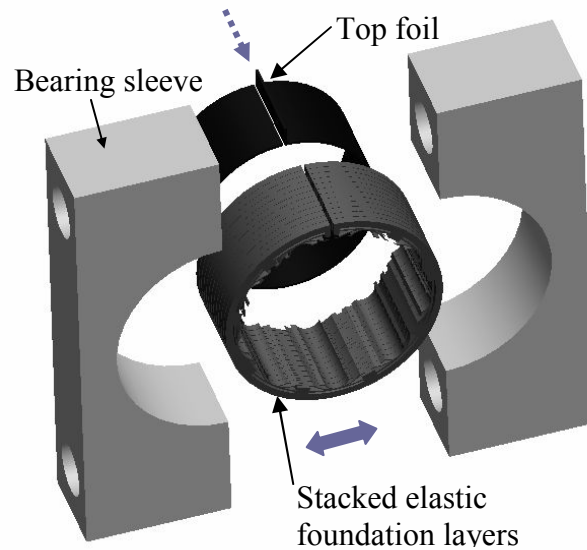


**Figure 4 Assembly Scheme of Mesoscale Foil Gas Bearing.**

Another important design feature of the manufactured mesoscale foil bearings is a self-generated preload. It is well-known that the lightly-loaded gas bearings are unstable due to large cross-coupled stiffness [14]. Traditionally external loading has been applied as a mechanism to increase the stability of fluid film bearings. Because external loading is not practical and very difficult in small rotating machines, the bearings should be designed such that they are self-preloading when installed on a machine. In the manufacturing process, the solid shell thickness is made different along the circumferential direction as exaggerated in Figure 5(a) & (b), via the lithography mask pattern.

Therefore, as illustrated in Figure 5 (c) & (d), when the two sub-bearing sets are arranged such that the top foil lips of the two bearings are  $180^\circ$  offset from each other, the total bearing assembly has a finite amount of self-generated preload caused by the preload offset in each sub-bearing. When the rig is assembled the rotor should be placed concentric with respect to the bearing sleeve. The preload from each sub-bearing is in opposite directions parallel to the plane connecting the two lips of the top foils, and the amount of each preload offset is the distance of the top foil center from the bearing sleeve center. Due to the preload offset, a pressure gradient develops such that each sub-bearing creates forces within the bearing set a finite distance apart. In other words, the net forces from each sub-bearing created by the preload are separated by a finite gap creating a coupled moment that acts to stabilize the bearing. The configuration is stable since a bearing pair generates equal and opposite moments that balance each other. The preload feature is useful to stabilize a lightly loaded bearing or to extend the stable operating range of a loaded bearing.

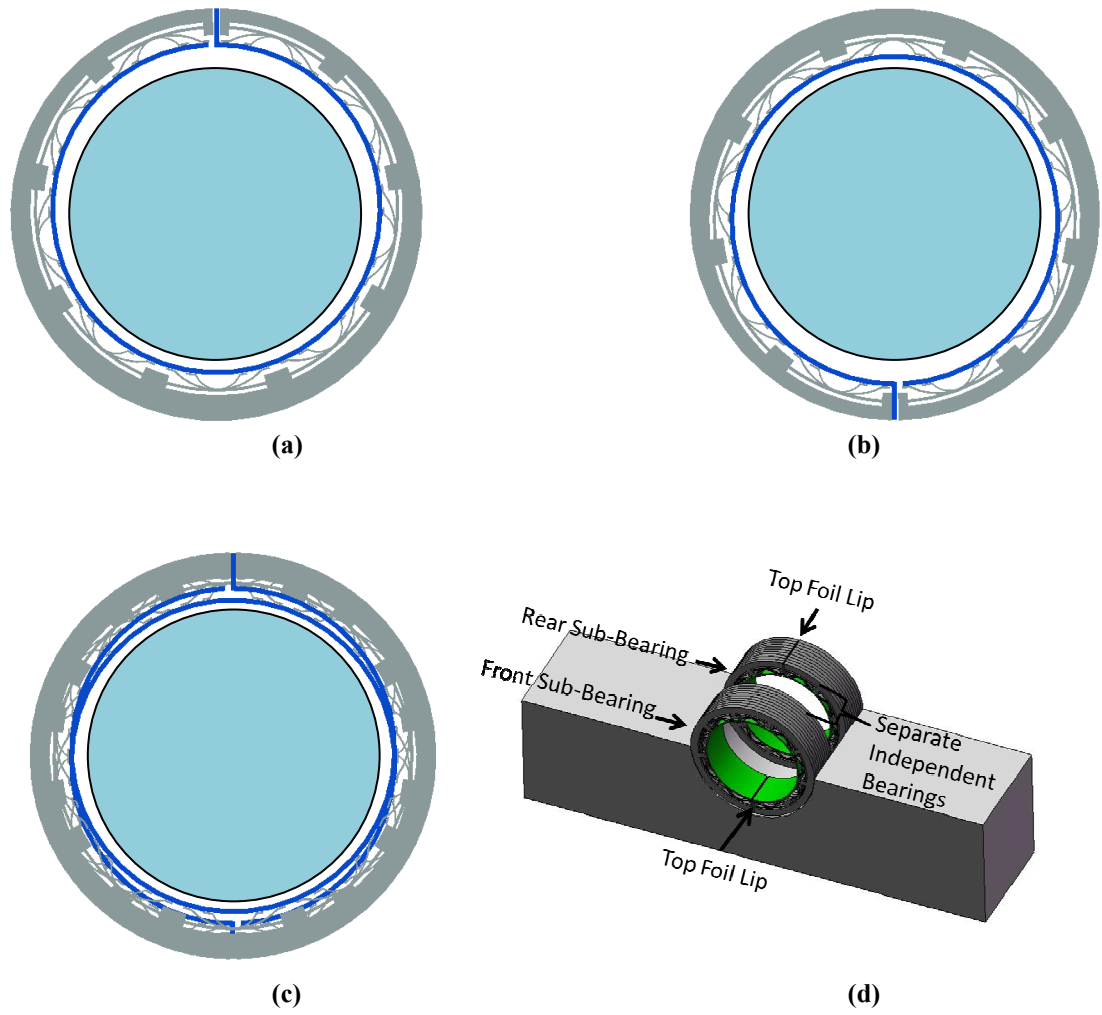


**Figure 5 Exaggerated Schematic of Elastic Foundation. Shows Different Shell Thickness Along Circumferential Direction. (a) Rear Half of Sub-Bearing (b) Front Half Sub-bearing (c) & (d) Back-to-Back Arrangement of Bearing Set.**

## CHAPTER V

### MICROFABRICATION

Since the foil bearing has a cross-section that is uniform along its length (two dimensional), one method that is feasible for creating the precise geometry required at a mesoscopic scale is the famous LIGA (Lithographie, Galvano-formung, Abformung) method [15] which means Lithography, Electroplating, and Molding in German.

#### **UV-Lithography**

The process of Ultraviolet (UV) Lithography requires a uniform and perpendicular [16] UV light source to provide the energy for reaction in materials called photoresists. Photoresist is a light-sensitive material used for applications such as creating the intricate patterns seen in Integrated Circuits (ICs). Silicon Wafers are often used as the working surface since they have unique properties that allow them to undergo many processing steps from high temperature baking to acid baths without failure.

The main purpose of the photoresist in IC manufacturing is to serve as shield for circuit materials like semiconductors and Cu electrical lines during the chemical etching steps. After processing SU-8 photoresist becomes a hard polymerized (plastic) material and it has resistance against many types of acids and solvents. Electroplating is a key step in the LIGA method, it is used to create a particular object e.g. foil bearings

foundations from the photoresist pattern by inserting metals into open spaces in the photoresist pattern.

The processing from UV-LIGA that is necessary includes a wet-etching of the Silicon Wafer for cleaning, baking to dehydrate wafer, metal evaporation, spin-coating SU-8 on wafer, soft baking, exposure, post-exposure baking, development, and electroplating. P-type Test Grade Silicon Wafers can be used as the processing stage for SU-8. Metal evaporation is used to create a conductive seed layer which is necessary to electroplate the Ni foil bearing elastic foundation in subsequent steps.

In order to electroplate materials into the plastic mold (photoresist pattern) the silicon wafer must be prepared in advance with an electrode layer for proper conduction during the electroplating step. A suitable metal combination is Cr with Au on top and a thickness on the order of 50 nm. However, much smaller thicknesses of both Cr and Au can be utilized as the electrode layer. In micro-injection molding applications, the metal that is deposited during the electroplating step of LIGA is not the final product but rather a master part for making plastic molds [17]. However, to make foil bearings metal i.e. nickel is frequently used therefore the LIGA method is utilized up to the electroplating step for making the proof of concept mesoscale foil bearings.

The UV-LIGA process should start with preparing the Silicon Wafer, cleaning and drying. After baking, a dry etch using O<sub>2</sub> plasma can ensure the dehydration of the surface and remove particulate matter. Several settings of the Reactive Ion Etcher must be recorded including pressure, power, time, and gas flow rate. The next stage of processing uses a metal evaporation chamber to coat Cr and Au layers on the Silicon.

Some of the important parameters that need to be recorded are the starting and ending deposition vacuum pressure since this can affect the uniformity of deposition. The evaporator takes advantage of the fact that in a vacuum the numbers of molecules as well as collisions are reduced allowing for a more uniform deposition of the intended metal. After the wafer is prepped with an electrode layer, spin-coating is done with a spin processor that allows for control of spin speed and time, both conditions must be recorded. The soft bake step is crucial to the rest of processing since it hardens the resin enough for the following step. Temperature at this step and the rate of change of temperature as well as time must be recorded. Exposure is done with a Mask Aligner which uses a vacuum to maintain contact between the photoresist and mask. Due to the vacuum a significant amount of pressure is placed on the photoresist during the exposure. Therefore, the conditions of the soft bake must be long enough to harden the photoresist to withstand this step. The Quintel Q4000 MA with an I-line light intensity of 12 mW is available in the Material Characterization Facility clean room at Texas A&M University. The exposure time must be recorded and will be used to determine the dose or energy density that is imparted on the photoresist in units of milli-Joules per unit area. The UV mask used in the exposure step is made from a 0.120in (30.48mm) glass membrane with a 75 $\mu$ m thick Cr film as the UV absorber. The temperature at each step and the rate of change of temperature as well as time must be recorded for the post-exposure bake. Light agitation is necessary for the development and the time must be recorded. Post-process cleaning must be done with Isopropyl Alcohol and dried with filtered air.

Detailed processing of UV lithography on 200 $\mu$ m thick SU-8 are as follows: Silicon wafer was cleaned in Piranha etching solution which consists of a 3:1 volumetric ratio of H<sub>2</sub>SO<sub>4</sub> and H<sub>2</sub>O<sub>2</sub> heated to 100°C for 1 hour, followed by O<sub>2</sub> plasma cleaning. As a seed layer for electroplating, 50 nm thick Cr and 50nm thick Au layers were evaporated on the silicon wafer using a BOC Edwards Auto 306 metal evaporation system. Because the adhesion of SU-8 is not good on the Au seed layer, an adhesion promoter, OmniCoat (from MicroChem, Inc.), was spin-coated on top of the Cr/Au seed layers to improve adhesion of the SU-8. 200 $\mu$ m thick SU-8 was spin-coated and soft-baked at 65°C for 7 minutes and 95°C for additional 39 minutes. Slow temperature ramp of 6°C /min. was used between 65°C and 95°C. Quintel Q4000 MA was used for UV exposure. The required dose was 315 mJ/cm<sup>2</sup> with an exposure time of 26.3 seconds and I-line intensity of 12mW/cm<sup>2</sup>. The post-exposure bake was done at 65°C for 5 min followed by additional baking at 95°C for 16 minutes. Slow temperature increase similar to the soft-baking was necessary. To reduce stress in the SU-8, the substrate was cooled slowly for about 12hrs after post-exposure bake. The SU-8 was developed for 16 minutes in SU-8 developer, cleaned with Isopropyl alcohol, and dried with filtered air.

A 1mm thick PMMA plating mold was also fabricated using X-ray lithography. Figure 6 is a photo of the fabricated X-ray mask. The dark areas without Au film in Figure 6 have images of the bearings to be manufactured. The X-ray mask was fabricated at Pohang University of Science and Technologies (POSTECH), and PMMA plating mold was developed through successive exposure to X-ray and development in a

G-G solution, which is composed of 60 vol.% of 2-(2-Butoxyethoxy)ethanol, 20 vol. % of Morpholine, 5 vol. % of 2-aminoethanol, and 15 vol% of de-ionized water.

After SU-8 or PMMA mold was manufactured, Ni was electroplated in a sulfamate bath. The Current density was  $10\text{mA}/\text{cm}^2$  at  $50^\circ\text{C}$  and further details may be found in the Microfabrication section. Figure 7 shows SEM images of the 1mm thick PMMA mold and optical image of 1mm thick elastic foundation layer made of Ni. The top foil made of  $75\mu\text{m}$  thick stainless steel sheet was manufactured using a hot-forming process at a temperature of  $500^\circ\text{C}$ .



**Figure 6 Photo of X-ray Mask. For Manufacturing the Mesoscale Foil Gas Bearings. Dark Area Is X-ray Transparent Material (Represents the Areas for Bearing Structure) and Bright Area Is the X-ray Absorber (Au Film).**

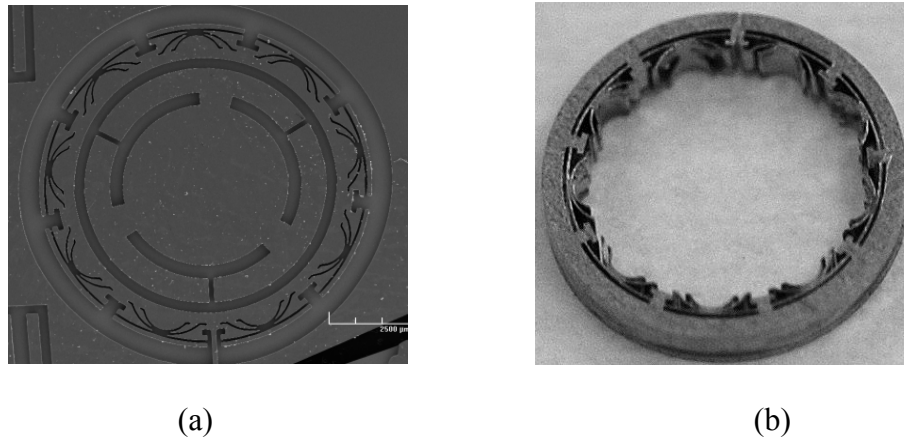


**Figure 7 SEM Image. Shows 1mm Thick PMMA Mold and Optical Image of Elastic Foundation Layer. (a) PMMA Mold (b) Elastic Foundation Layer.**

### **Electroplating**

Nickel coatings are usually utilized for their material properties and for decorative purposes. It has many different useful properties including corrosion resistance, high hardness, and long wear capability as well as magnetic properties. These properties have brought nickel great attention and are often applied to improve the surfaces properties for different applications. The electroplating system for the mesoscale foil bearing consisted of the following equipment:

1. Thermo Electron Corp. microprocessor controlled precision water bath heater, Model # 2841
2. Acrylic cover, 1 in. thick, was used for heat insulation
3. Polyethylene electroplating 3 gal tank
4. Agilent DC power supply ( Model # E3610A)

#### 5. Talboys, Model 101, electric motor driven stirrer

Figure 8 presents the major chemical reactions in the electroplating tank. In order to maintain a constant temperature a 1 in. thick acrylic plastic cover is used both for heat insulation and its inert nature. The electroplating system consists of an acrylic cover and wafer holder, a large polyethylene electroplating tank, an Agilent DC power supply (Model # E3610A), and a Talboys electric motor driven stirrer.

The Ni anode is oxidized at the anode and associated with the sulfamate solution, thereby replenishing the  $\text{Ni}^{2+}$  ions. The cathode or substrate that is desired to be plated attracts the  $\text{Ni}^{2+}$  ions due to its negatively charged surface. The excess of electrons at the surface of the cathode reduces the  $\text{Ni}^{2+}$  ions into a solid metal form onto the cathode. The reaction occurs with a pair of electrons governed by equation 4.1 depositing metal Ni onto the wafer.

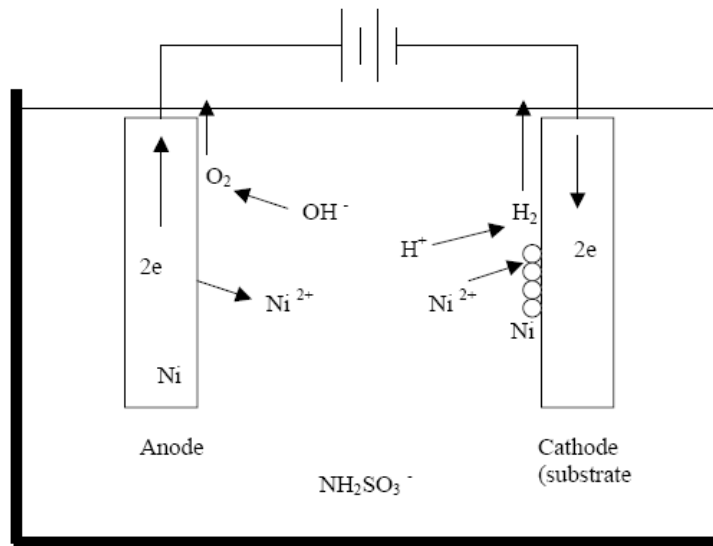


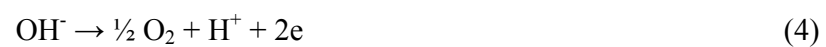
**Figure 8 Electroplating [18]. Schematic of the Chemical Reaction and Essential Components.**

The main reactions at the cathode and anode are listed below:

Cathode Reactions:



Anode Reactions:



When the dissolution efficiency of the Ni anode becomes 100% then the hydroxyl ions ( $\text{OH}^-$ ) are no longer dissolved in the water present in the electroplating bath. If the dissolution reaches 100% then oxygen is evolved at the anode Eq. (4) instead of the Nickel dissolution. Then amount of the hydroxyl ions will increase. The electroplating will come to halt in this scenario because the anode is no longer being dissolved, therefore no  $\text{Ni}^{2+}$  ions are supplied to the cathode.

To counter the effects of this type of dissolution sodium hydroxide,  $\text{NaOH}$ , was used to increase the pH when the solution pH became less than 3.5 and a diluted sulfamic acid,  $\text{H}_3\text{NO}_3\text{S}$ , was used to decrease the pH of the solution if the pH became greater than 4. A wetting agent was also used to reduce the surface tension of the nickel sulfamate solution and yield good product quality. This is a common practice for electroplating at micro-scale. The working pH 3.7 provided a sufficient electroplating solution with smooth Ni plating. Table 1 provides the amounts of each chemical in the working solution.

**Table 1 Chemical Quantities for Nickel Electroplating.**

Component	Amount per 1L solution
Nickel sulfamate( $\text{Ni}(\text{NH}_2\text{SO}_3)_2$ ) 50% aqueous solution	450ml (78g $\text{Ni}^{2+}$ ions/L)
Sodium Lauryl Sulfate	1g
Boric Acid ( $\text{H}_3\text{BO}_3$ )	37.5g
DI water	To final volume
pH	3.7
Temperature	50°C
Current density	10mA/cm <sup>2</sup>

**Process Control: Current Density**

A critical element that significantly impacts electroplating and the finished materials produced is the current density. Current density or the current per unit area is commonly expressed in units of mA/cm<sup>2</sup>. The thickness of an electroplated material is heavily dependent on the current density. The amount of the electroplated metal is of great concern and is perhaps the most important parameter in terms of its effect on the outcome of micro-parts. One key for properly determining the current density is to accurately determine surface area of the substrate with the polymer electroplating mold. This is also one of the challenges, since even the minor adjustments in the lithography process can affect the surface area and a researcher's ability to accurately know the

amount of surface area to be electroplated. However, due to the size of the parts in a polymer electroplating mold it is often sufficient to use directly the substrate geometry without loss of significant accuracy. Faraday's Law for the electroplating is expressed by the following equation [19]:

$$m = \frac{\eta_c M}{n_e F} It \quad (5)$$

Where  $m$  is mass of electroplated nickel in grams,  $M = 58.7\text{g/mol}$  is the molecular weight of nickel,  $n_e = 2$  is the number of electrons in the reduction reaction for nickel ions,  $F = 96488\text{C/mol}$  is Faraday's constant,  $\eta_c$  is cathode efficiency which is often taken to be 0.95-0.97,  $t$  is time, and  $I$  is the total current. The same equation may be expressed per unit density as

$$d = \frac{\eta_c M}{n_e F \rho} Jt \quad (6)$$

In this equation  $\rho=8.9\text{ g/cm}^3$  is the density of the plating material,  $J$  is the current density in  $\text{mA/cm}^2$ . If  $\eta_c = 1$ , then the approximate electroplating rate is  $0.2\ \mu\text{m}/\text{min}$  and the time necessary to electroplate  $200\ \mu\text{m}$  thick nickel into a SU-8 electroplating mold is close to 17 hours. Another issue that arises is the edge effect which causes a deviation from the ideal values in the electroplating time. It is well known that the

current density is not uniform throughout any material. This is due in part to the inhomogeneity present in all raw materials and the location of electrical contact of the power supply lead. The current density is higher closer to the edge of the substrate and the higher current density causes a local increase in the plated material's growth rate. Therefore the areas of interest are not plated in the idealized time frame given by Eq. (6). The samples are over plated for about 20 hrs and then polished to the intended thickness.

### **Purification of Nickel Solution**

Before a plating solution is prepared it is necessary to execute a purification procedure. Without purification contaminants may lead to unexpected chemical reactions and unreliable electroplating results. According to the supplier's manual and their years of electroplating specialty [20].

Purification procedures which are suitable for laboratory use are:

1. Fill tank with distilled water to 2/3 of the desired volume.
2. Heat bath up to 50 °C .
3. Add boric acid into the bath while continuing to stir the solution (At this time other chemicals can be added).
4. Add 2g/L of activated carbon, agitate for 2 hours and filter the solution.
5. Adjust the pH to 5.5-5.8, thoroughly agitate the solution for at least 2 hours.
6. Dummy the solution. Steel sheets are used as the cathodes. An average deposition current of 0.5A/dm<sup>2</sup> was maintained. The electrolysis should

continue until the appearance of the sample is acceptable. During the procedure, the solution should be well agitated.

7. Remove the dummy cathodes and adjust the pH of the solution by adding diluted acid again until it is within the proper range.

## CHAPTER VI

### CHALLENGES OF MICROFABRICATION

Although the processing steps for UV lithography using SU-8 are well known every step must be customized to fit the application [21]. In sequential processing the result of a current step can only be as good as the previous step. Fortunately, there is a fairly good understanding of how each step affects the final state of the SU-8 epoxy.

#### **Photoresist Processing**

The first step in Lithography processing is to prepare the Si wafer with a wet etch. The wet etch roughens the surface of the wafer while removing any particulate matter, both are advantageous for metal evaporation.

After the wet etch step, the Si wafer is baked this helps to dehydrate the surface which is beneficial for evaporation as well. If the Si wafer is rinsed without being dried long enough or baked then the uniformity of deposition of electrode seed layer of the Si wafer will be adversely affected due to the moisture on surface and its interaction with the evaporated metal. The polymer layers created from SU-8 is directly proportional to the spin speed of the spin processor and the exact thickness will depend on the viscosity of the photoresist. Manufacturer recommended programs for spin-coating work well.

After coating the wafer with a specific thickness of a honey-like SU-8, the next step is soft-baking, one of the most important steps. The final product can easily be ruined if the soft bake is done for too short a time or on an improperly leveled surface. SU-8 is baked beyond the glass transition temperature during soft baking step and this

may cause the polymer to re-flow into a non-uniform shape. Additionally, if the baking is not done for a long enough period SU-8 will be full of solvents and not strong enough for subsequent processing steps. Removal of solvents will cause the molecules of the polymer to be more tightly packed and increase the crosslink density. Both are beneficial to the stiffness of the SU-8 and reduce stress [21, 22] in later stages including Post Exposure Bake (PEB).

Exposure is another step that can significantly impact the pattern transfer. The Power per unit is referred to as a dosage, and without the correct dose the amount of cross-linking polymer could be too much or too little affecting the electroplating mold. If there is too much energy this is called an overdose and the opposite is an under dose. Overdose results in excessive cross-linking and can lead to a “T-top.” As the name implies the SU-8 will cross-link more toward the top of the microstructure where the UV source originates causing a T-like shape. Under dosage will result cross-linking of the SU-8 only near the surface. If that occurs a blurring effect happens in the development stage due to randomized un-exposed SU-8 that is susceptible to dissolution in the developer.

PEB is one of the simplest steps but a crucial point is to execute this step immediately after exposure. Using gradual ramp rates between temperatures is good for reducing thermal stress that can deform the polymerized photoresist’s shape. Thermal stress during PEB causes wrinkles especially in over exposed SU-8. Finally, a slow ramp down from the baking temperature of about 12 hrs is necessary to reduce thermal stress after PEB and helps with cracking of sharp features.

## **Electroplating**

Besides current density, important quantities for electroplating include temperature, purity of water, and pH [19]. After developing a working solution, controlling pH is important to continue electroplating in a predictable and repeatable way. Cracking and pitting of the Ni plating may occur outside the recommend pH range. Any pH variation may result in lower cathode efficiency. In the electroplating system an Oakton Instruments pH tester, Model # pHTestr2, was used to measure the pH number.

The operating temperature is another of the primary ingredients that control the quality of the electroplating deposition and should be maintained in the recommended range to keep the miscibility of the solution. The suggested working temperature for nickel deposition is 38 to 60 °C. Therefore, the Thermo Electron Corp. precision water bath's ability to provide an isothermal working condition of 50 °C is instrumental for the electroplating system.

Finally the quality of the water used to replenish the water loss due to evaporation can either help to maintain the solution or introduce unpredictable reactions from impurities. The effects of evaporation at 50°C or other higher temperature in the recommended range increase the evaporation rate as compared to room temperature.

## CHAPTER VII

### TEST RIG DESIGN

The test rig and its major components are of great importance for determining the performance and also validating the numerical simulation results. This chapter describes the components and the how they relate to each other as well as the overall test rig.

#### **Design Description**

Determining the performance of the foil bearing is achieved using a simple impulse turbine including a bearing housing, shaft supported by the foil bearings, turbine, and turbine shroud as well as displacement sensors and tachometer. The performance characteristics may be determined using the unfiltered and filtered peak to peak measurement of vibration, the frequency of rotation, and time. Orbit plots, coast down performance, and onset of instability can be determined using a test rig as shown in Figure 9, the basic concept of the design. The fiber optic sensors need to be positioned orthogonal to each other which places a constraint on many of the contact surfaces to be planar. Each fiber optic sensor is held in place with an adjustable holder as shown in Fig. 10. The mounted holders as well as base plate they are attached to must be level and mate seamlessly with the parts they contact in order for the sensors to be orthogonal. The tachometer captures speed and time data which are the remaining parameters necessary for measurement.

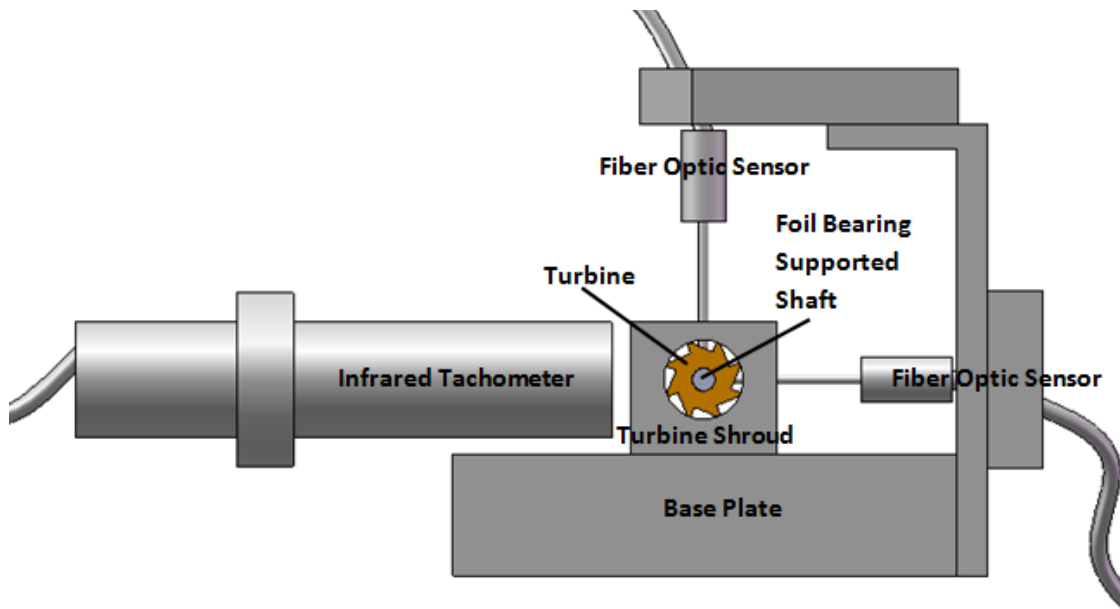


**Figure 9 Test Rig and Experimental Setup. Used for Vibration Measurement and Determination of Bearing Performance.**

### **Design Requirements**

1. Measure the amplitude of vibration in two orthogonal axes at various speeds.
2. Locate the position sensors orthogonal from each other in any location along the shaft.
3. Provide full enclosure of moving parts while having slots for various types of measurement.
4. The test rig should accommodate different size bearings and rotors.
5. Ability to be powered from standard  $\frac{1}{4}$  inch tubing compressed air source with appropriate pressure control.
6. Provide adjustable axial support.

The final iteration of the test rig in SolidWorks is shown in Figure 10. It is common practice to measure the displacements in a particular plane resulting from the shaft rotation. All the parts of the test rig are made for that purpose. Although it may appear like an obvious setup, planning and attention to detail is necessary to make all the parts work together and has to be carefully considered.

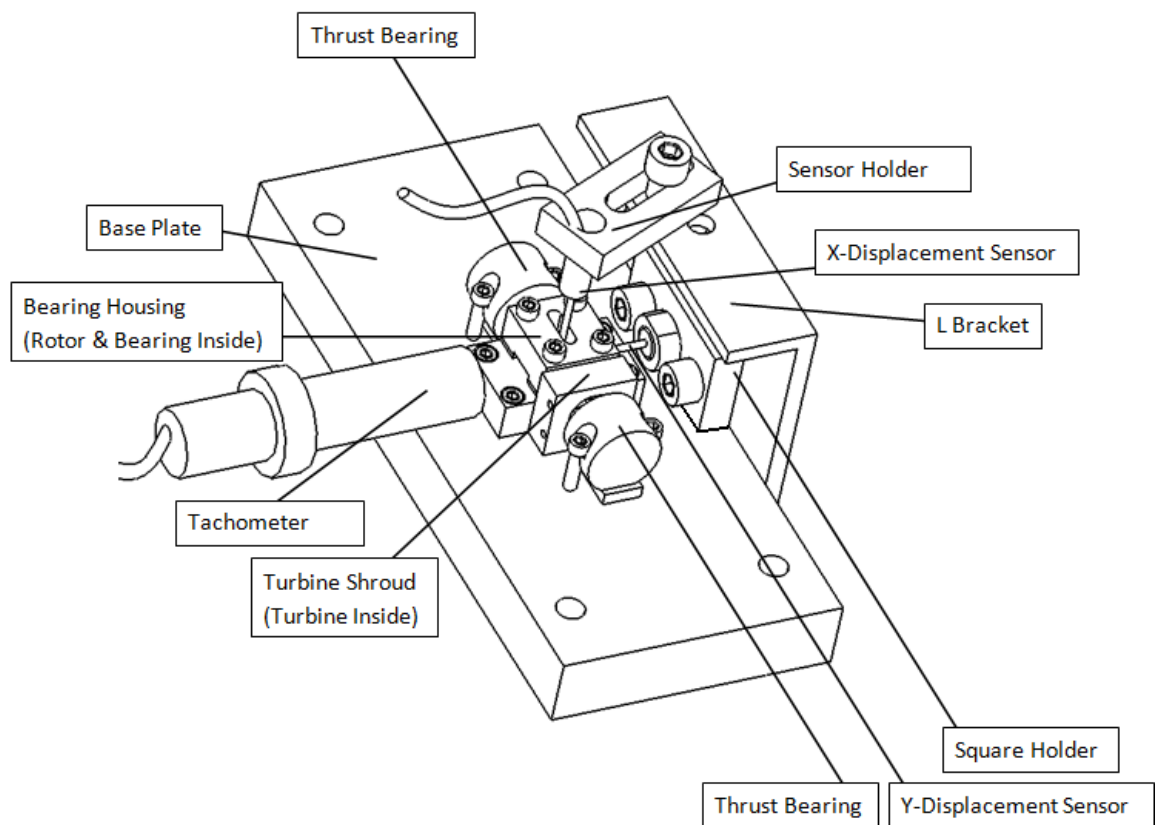


**Figure 10 Test Rig, General Layout of Components.**

The Turbine and Turbine shroud shown in Figure 11 must have a very close fit between the turbine blade and the turbine shroud central thru-hole. The diameters of both are equal at 0.43in. Otherwise the test rig cannot utilize the maximum potential of the air pressure. A custom made reamer was used to achieve the diameter since it is not a standard size.

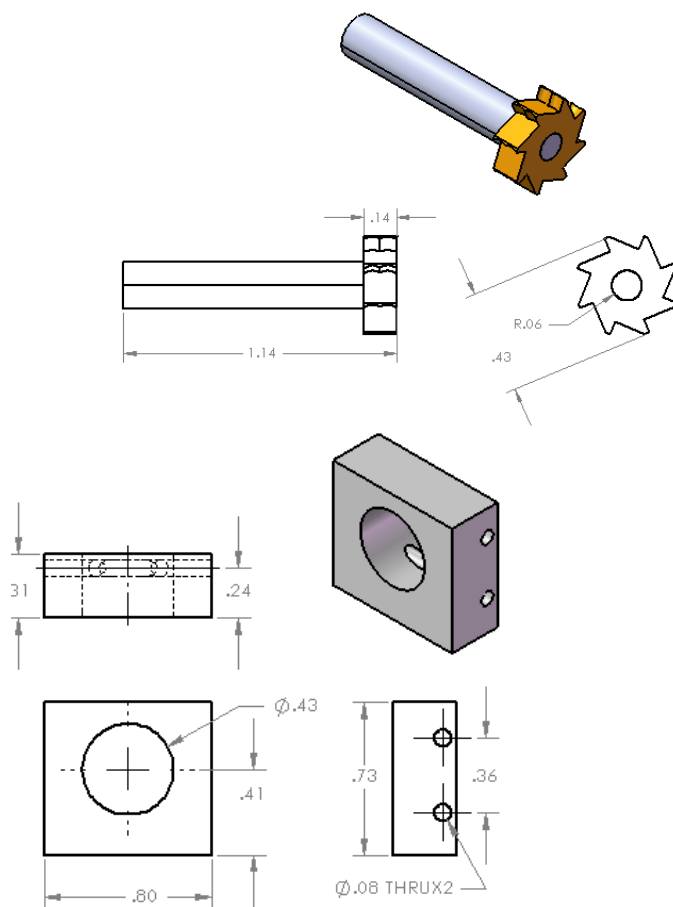


**Figure 11 Turbine and Turbine Shroud Dimensions (units: inches). Not All Dimensions Are to the Precision Used.**

The Base Plate and Bearing Housing must have a close alignment to the four tapped holes in the center of the Base Plate and the clearance holes in the bottom half of bearing housing to mate together, Figure 12. The assembly of these two parts along with the turbine, turbine shroud, and bearings are the basis for the placement of all the other parts in the test rig. Since the sensor holders are adjustable, once the assembly is finished the sensors can be placed at a point of interest for taking vibration and speed data.

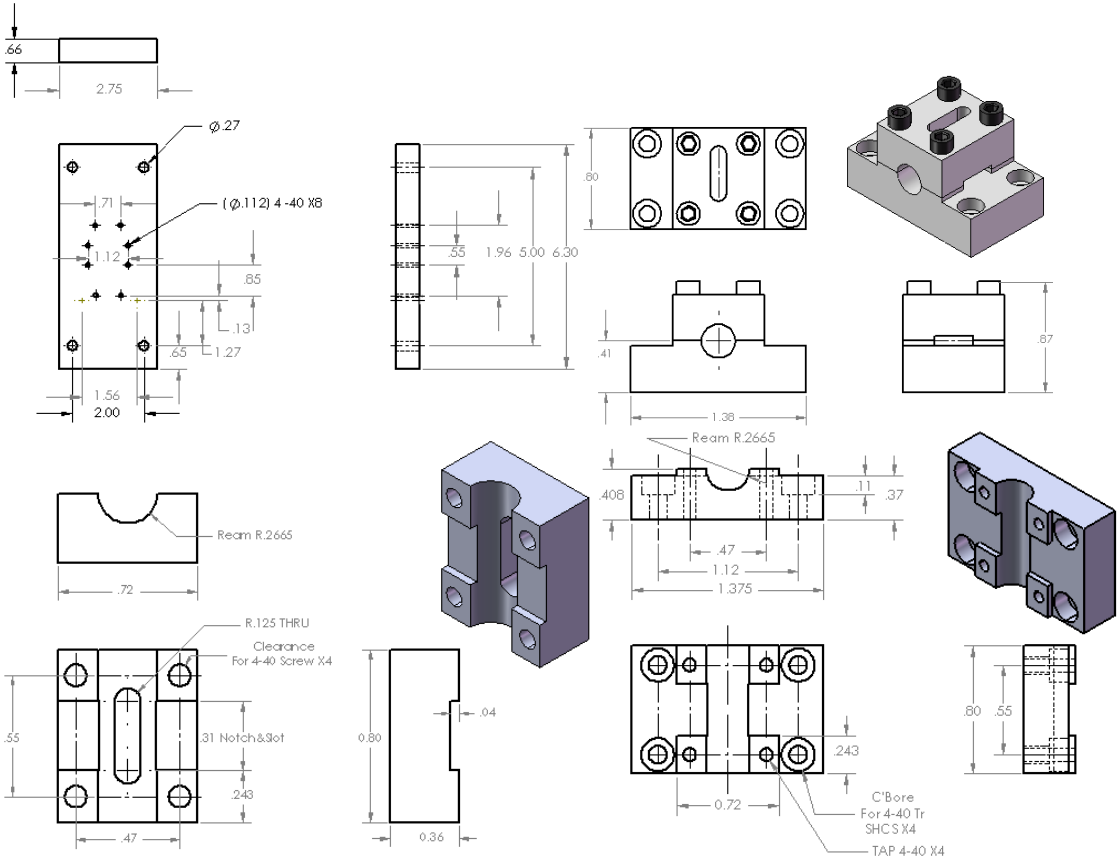


**Figure 12 Base Plate and Bearing Housing Dimensions (units: inches). Base Plate (top left), Bearing Housing (top right), Top of Bearing Housing (bottom left), Bottom of Bearing Housing (bottom right) Dimensions (units: inches). Not All Dimensions Are to the Precision Used.**

The thrust bearings, Figure 13, are used to provide a rigid support in the axial direction such that it is reasonable to assume no motion occurs in the axial direction which is assumed in the simulation section. The clearance grooves in the side of the thrust bearings are used to mate with base plate while the holes in the cylindrical tip are used to apply and air cushion for the rotor of the turbine.

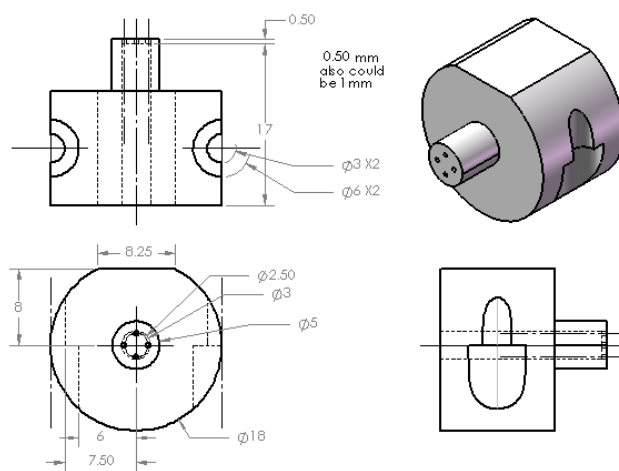


**Figure 13 Thrust Bearings Dimensions (units: inches).The thrust bearings where made as identical as possible. Variation was a magnitude of about 1-2 mils. Not All Dimensions Are to the Precision Used.**

The L-Bracket functions to keep the fiber optic sensors perpendicular. It also allows the holder part in the Y-direction to translate a short distance in a plane perpendicular to the sensor axis. Set screws are used in both holders which enables adjustment along the axis of the sensor. The X-Sensor holder can move in a plane perpendicular to the sensing axis since it has a groove that allows translation and rotation, Figure 14.

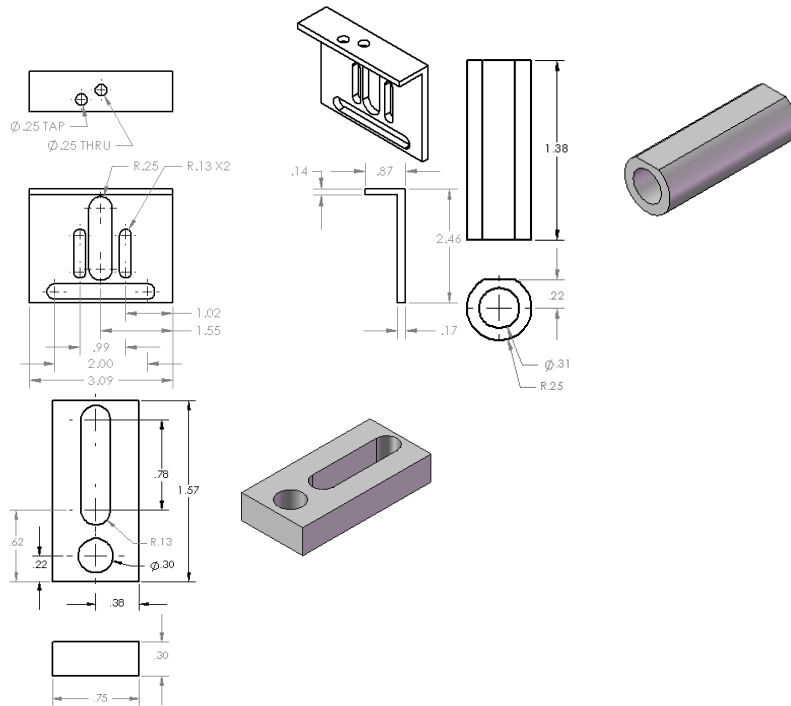


**Figure 14 Sensor Holder Parts (units: inches). L-Bracket (top left), Y-Sensor Holder (top right), X-Sensor Holder (bottom left), and Square Holder (bottom right) Dimensions (units: inches). Not All Dimensions Are to the Precision Used.**

The Sensor holders are the backbone of the measurement. The surfaces in contact with the fiber optic sensor must be smooth, precise, and bur free in order to hold the sensor in a repeatable manner. Particular care was made in making the L-Bracket which had less than 0.1 degree of slope on either face according to the measurement from the Smart Tool Digital Angle Level. Similar measurements were made on all mating surfaces and machining adjustments were done to ensure measurements of levelness of less than 0.1 degree of slope.

Using level measurements, drawings, and assembly checks the test rig was designed and re-designed to ensure it could meet all requirements. Figure 15 shows all the machined parts of the test rig:

1. The Philtec fiber optic displacement sensor, Model #D20-B1R, with a  $0.004\mu\text{m}$  and  $0.08\mu\text{m}$  near and far field resolution was selected to measure the amplitude of vibration.
2. The Monarch IRS sensor (IR tachometer), Model # IRS-P, with a speed range of 1-999,990 RPM was selected for measurement at various speeds.
3. Smart Tool Digital Angle Level with a 0.1 degree resolution was used to ensure mated faces of sensor holding parts were orthogonal for locating the sensors perpendicularly at any location along the shaft.
4. A closed bearing housing and turbine shroud served the dual purpose of support for their respective contents and shielding the test from any crashes of the rotor. The bearing housing also has slots for measurement that allowed for measurement along the shaft.
5. The modular design also accommodates different bearing housings which can be used with different size bearings and rotors.
6. All pneumatic fittings have conversion connectors for standard  $\frac{1}{4}$  inch tubing or they are already standard  $\frac{1}{4}$  inch tubing so that they may be powered from standard compressed air sources.
7. Two air thrust bearings powered from standard  $\frac{1}{4}$  inch tubing provide adjustable axial support.

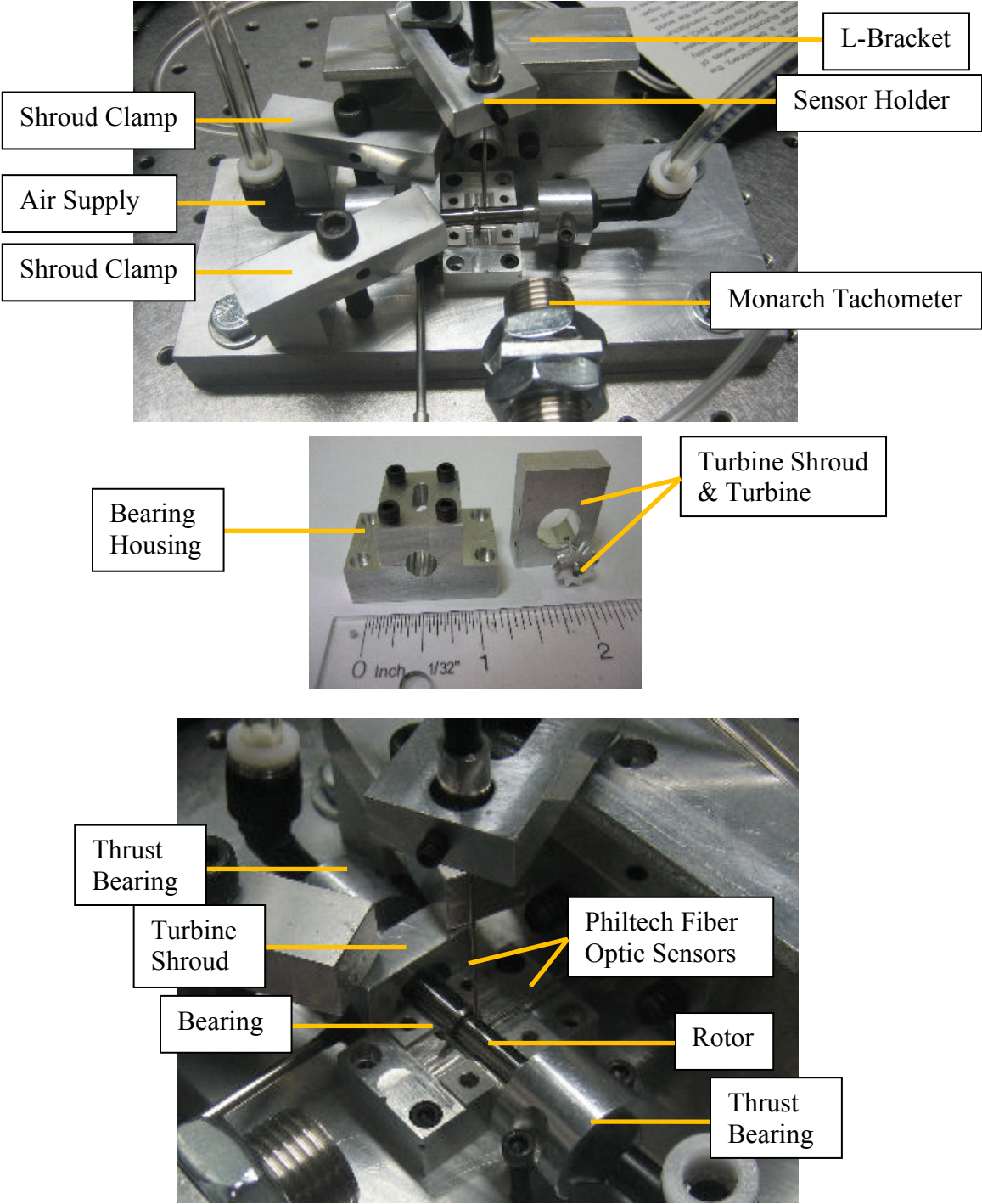


Figure 15 Components of the Test Rig.

## CHAPTER VIII

### NUMERICAL SIMULATION

To understand the dynamic behavior of the mesoscale foil gas bearing, a mathematical model was developed to simulate the rotordynamic behavior of a rotor supported by the mesoscale foil gas bearings.

#### **Model of Elastic Foundation**

Although the layers are not bonded, the total elastic foundation is assumed to be one piece with a length corresponding to the sum of each elastic foundation layer. In the computational model for the pressure calculation, the bearing surface (on the top foil) is modeled with multiple grid points along the circumferential and axial directions. Note that the number of grid points along the axial direction does not have to be the same as the number of elastic foundation layers because the elastic foundation is assumed one piece in physical model. Because the pressure is different along the axial direction, the elastic foundation undergoes different deflection along the axial direction. Therefore, for the simplicity of computational model, it is assumed that the elastic foundation (one piece in physical model) can be modeled as multiple independent strips (layers) corresponding to the number of computational grid points along the axial direction, and each strip provides independent elastic support to the top foil. The thickness of each elastic foundation layer can be chosen such that the number of layers within the foundation matches with the number of grid points along the axial direction. However, because different bearing design (and fabrication method) can have different thickness of

elastic foundation layers and total bearing length, it is more convenient to separate the physical and computational domains.

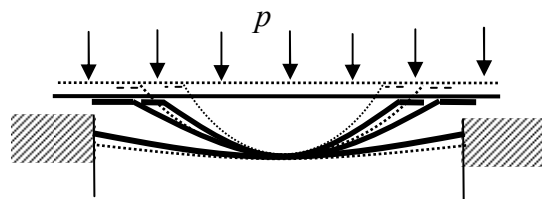
Because the elastic foundation is modeled as multiple strips, each bump set within the strip is consisted of two bumps (IB and OB) with small contact patches with the top foil and one partial arc beam (AB) fixed to the structure (See Figure 2). The stiffnesses of IB, OB, and AB can be calculated using elementary beam theory [23] assuming the contact patches of IB and OB are free to move. The thickness of all the beam structures is  $50\mu\text{m}$ .

Figure 16 shows presumed motions of one bump set under dynamic pressure through the top foil. The simplified model represented by the two spring-viscous dampers assumes that the top foil and elastic foundations are mass-less. Dotted lines and curves represent the structure and the top foil before deflection and solid lines represent the deformed shapes. Design of the mask in Figure 6 was made such that the distances between individual spring-dampers are nearly equally-spaced. Because each bump set is modeled as two spring-dampers, the equivalent stiffness can be found from the following equation:

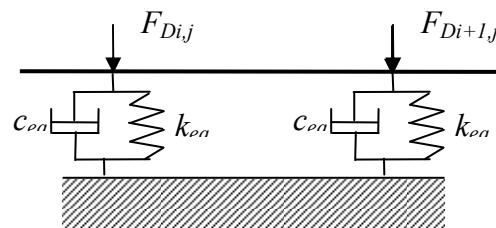
$$\frac{1}{2k_{eq}} = \frac{1}{(k_{IB} + k_{OB})} + \frac{1}{k_{AB}} \quad (7)$$

Where  $k_{AB}$  is a stiffness of AB,  $k_{IB}$  and  $k_{OB}$  are the stiffnesses of IB and OB, respectively. Many researches in macroscale foil bearings [24-29], model the bump foils as spring-viscous damper with equivalent damping coefficient,  $c_{eq} = \gamma_b k_{eq} / \omega$ , assuming

the bump motion is sinusoidal by imbalance excitations. The structural loss factor can be found experimentally and many experimental studies on damping measurements of the bump foils [24, 25, 27] show that the loss factor is in the range of 0.15~0.25 depending on design. Because the shapes of the IB and OB are similar to those of macroscale bump foils, structural loss factor of 0.2 was assumed in the simulations.



(a)



(b)

**Figure 16 Elastic Foundation Schematic. (a) Presumed motions of one bump set (b) Assumed Two Spring-Damper Models for Each Bump Set.**

Adopting the spring-viscous damper model, the equation of motion for each spring-damper is

$$c_{eq} \dot{\delta}_{Di,j} + k_{eq} \delta_{Di,j} = F_{Di,j} \quad (8)$$

The proposed model would render a negative film thickness at the bearing edges where net pressure becomes zero whenever the bearing is loaded beyond the original clearance. Therefore, the top foil deflections at the edge region adopt a linear extrapolation from the values evaluated near the edge of the bearing. The accuracy and appropriateness of the independent elastic support model along the axial direction and the extrapolation toward the edge regions were validated in previous studies on macroscale foil gas bearings [24, 27].

### **Model of the Hydrodynamic Pressure on the Top Foil**

The dynamic forces,  $F_{Di,j}$ , can be found by solving a simplified Navier Stokes equation applied to thin gas film, i.e. Reynolds equation [30] given by

$$\frac{\partial}{R^2 \partial \theta} \left( \frac{ph^3}{12\mu} \frac{\partial p}{\partial \theta} \right) + \frac{\partial}{\partial z} \left( \frac{ph^3}{12\mu} \frac{\partial p}{\partial z} \right) = \frac{R\omega}{2} \frac{\partial}{R \partial \theta} (ph) + \frac{\partial}{\partial t} (ph) \quad (9)$$

where  $\mu$  is viscosity,  $p$  is pressure,  $h$  is local gas film thickness,  $\omega$  is angular velocity of the rotor,  $\theta$  is circumferential coordinate described in Fig. 8,  $z$  is axial direction, and  $x$  is the circumferential direction of the unwrapped bearing. Equation (9) can be non-dimensionalized as

$$\frac{\partial}{\partial \theta} \left( PH^3 \frac{\partial P}{\partial \theta} \right) + \frac{\partial}{\partial Z} \left( PH^3 \frac{\partial P}{\partial Z} \right) = \Lambda \frac{\partial(PH)}{\partial \theta} + 2\Lambda \frac{\partial(PH)}{\partial \tau} \quad (10)$$

where  $\Lambda = \frac{6\mu\omega}{p_a} \left( \frac{R}{C} \right)^2$ ,  $\theta = \frac{x}{R}$ ,  $Z = \frac{z}{R}$ ,  $\tau = \omega t$ ,  $H = \frac{h}{C}$ , and  $P = \frac{p}{p_a}$ .  $\Lambda$  is the bearing

number,  $R$  is the bearing radius,  $C$  is a nominal radial clearance of the bearing, and  $p_a$  is an atmospheric pressure. The geometry of the bearing, journal, and housing is shown in Figure 17 along with a schematic of the grid. The global coordinates are  $X$ ,  $Y$ , and  $\theta$  and the journal and Bearing radius are  $R_j$  and  $R$ , respectively.

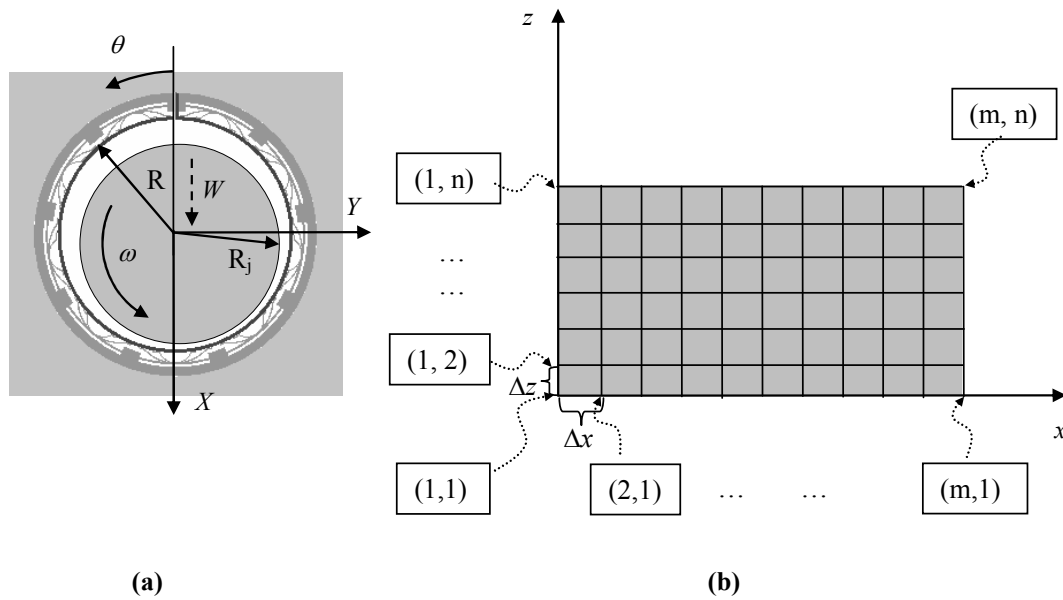


**Figure 17 Coordinate Systems for Analyses. (a) Orbit Coordinate System (b) Unwrapped Bearing Grid and Coordinate.**

As described earlier, assembled bearings have a hydrodynamic preload along vertical direction in Figure 9. If the preload offset distance is denoted as  $r_p$ , local film thickness, Eq. (11), at front and rear sub bearings considering rotor centrifugal growth can be described as

$$\begin{aligned} H(\theta, Z) &= 1 - r_g / C + (\varepsilon_x + r_p / C) \cos \theta + \varepsilon_y \sin \theta + W(\theta, Z); & 0 < Z < 1/2 \\ H(\theta, Z) &= 1 - r_g / C + (\varepsilon_x - r_p / C) \cos \theta + \varepsilon_y \sin \theta + W(\theta, Z); & 1/2 < Z < 1 \end{aligned} \quad (11)$$

Where  $W(\theta, Z)$  is a normalized top foil deflection by clearance  $C$ ,  $\varepsilon_x$  and  $\varepsilon_y$  are non-dimensional rotor eccentricity in X- and Y-direction, respectively,  $r_g$  is a rotor centrifugal growth. The front sub bearing ( $0 < Z < 1/2$ ) has a preload in +X direction while rear sub bearing ( $1/2 < Z < 1$ ) has a preload in -X direction. The rotor centrifugal growth can be predicted using

$$r_g = \frac{R\rho\omega^2}{4E} \left[ R_i^2(\nu + 3) + R^2(1 - \nu) \right] \quad (12)$$

Equation (12) was derived from plane stress model of rotating cylinder [23] with inner radius  $R_i$  for rotor material density  $\rho$ , Young's modulus  $E$ , and Poisson's ratio  $\nu$ , but agrees very well with finite element results [13] because rotor is not constrained along the axial direction.

The top foil deflection term  $W(\theta, Z)$  needs attention. Because the thin top foil is supported by multiple elastic supports separated by a certain pitch,  $p_b = 4\Delta x$ , as depicted

in Figure 18, the top foil undergoes sagging between the elastic supports as shown. In the figure, a local sagging term,  $v_{Di,j}(\zeta)$ , is defined with respect to local coordinate  $\zeta$  attached to the point where  $F_{Di,j}$  is applied.

The distance between a set of equivalent stiffness and damping nodal points is constant and referred to as the pitch of the bump. The pitch,  $4\Delta x$ , is a constant for a particular grid size as shown in Figure 18 and defines the full range of the local variable,  $\zeta$ . The variable,  $x$ , is the circumferential coordinate while the variable,  $z$ , is the axial coordinate reference of the unwrapped bearing grid, Figure 17 The grid spacing,  $\Delta x$  and  $\Delta z$ , is dependent on the grid size,  $m$  (number of grid points along  $x$  axis) by  $n$  (number of grid points along  $z$  axis).

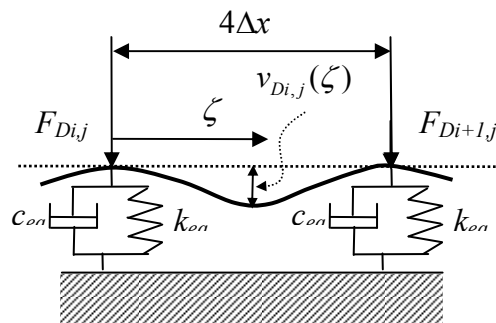


**Figure 18 Exaggerated Description of Top Foil Sagging.**

Because the top foil sagging effect is considered, nodal points for pressure calculations are assigned as shown in Figure 19, where three computational nodal points are assigned between two elastic supports.

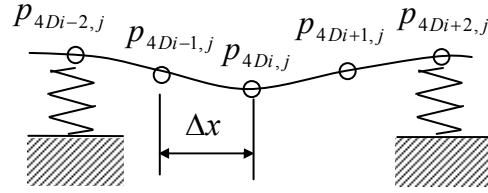


**Figure 19 Index for Nodal Pressures.**

In this paper, a simple analytical sagging model proposed by Kim and Park [31] was adopted to find the sagging term,  $v_{Di,j}(\zeta)$ , and total top foil deflection. They showed that their simple sagging model agrees very well with experimental results. Following the model in [27], the total force acting on a single bump can be given by

$$F_{Di,j} = \frac{\Delta x \Delta z}{24} \begin{pmatrix} -p_{4Di-5,j} - 2p_{4Di-4,j} + 12p_{4Di-3,j} + 26p_{4Di-2,j} \\ +26p_{4Di-1,j} + 26p_{4Di,j} + 12p_{4Di+1,j} - 2p_{4Di+2,j} - p_{4Di+3,j} \end{pmatrix} \quad (13)$$

Furthermore, the maximum sagging amount of the top foil at the center between the two elastic supports can be found as

$$v_{Di,j}(2\Delta x) = \frac{\Delta x^4 \Delta z}{15EI} \left( 3p_{4Di+2,j} + p_{4Di+1,j} + 1.5p_{4Di+3,j} + 3p_{4Di-2,j} + 1.5p_{4Di-3,j} + p_{4Di-1,j} - p_{4Di,j} \right) \quad (14)$$

$$\alpha_f = \frac{\Delta x^4 \Delta z}{15EI} \quad (15)$$

Where  $\alpha_f$ , is the sagging coefficient. Once the sagging function,  $v_{Di,j}(\zeta)$ , and deflection of elastic foundation,  $\delta_{Di,j}$ , have been calculated, the total top foil deflection at location  $\zeta$  can be found as

$$w_{Di,j}(0) = \delta_{Di,j} \quad (16)$$

$$w_{Di,j}(2\Delta x) = \delta_{Di+1,j} \quad (17)$$

$$w_{Di,j}(\zeta) = \left( 1 - \frac{\zeta}{2\Delta x_1} \right) \delta_{Di,j} + \frac{\zeta}{2\Delta x_1} \delta_{Di+1,j} + v_{Di,j}(\zeta) \quad (18)$$

Finally, normalizing the terms in Eq.(18) by the nominal clearance  $C$  yields the top foil deflection term,  $W(\theta,Z)$ , in Eq. (11). Detailed descriptions of the analytical top foil sagging model and mathematical formulation for Eqs. (16)~(18) can be found in [31].

The importance of the sagging deflection from Kim and Park in the context of the mesoscale foil bearing may be determined by comparing the sagging coefficients in both cases. Since the moment of inertia,  $I = \frac{1}{12} \Delta z t_b^3$  the sagging coefficient may be simplified as

$$\alpha_f = \frac{12\Delta x^4}{15Et^3} = \frac{3.125 \times 10^{-3}}{E} \frac{p_b^4}{Ct_b^3} \propto \frac{p_b^4}{Ct_b^3}$$

(19)

The sagging coefficient,  $\alpha_f$ , for the mesoscale foil bearing in this paper is  $3.3 \times 10^{-3}$  times that of macro scale foil bearing introduced in [31]. This result shows that the sagging effects are less significant in the case of the mesoscale bearing, and could be assumed negligible. Assuming both foils are made from the same materials, it is clear from Eq. (19) that the sagging effects will be more significant with a longer bump pitch and thinner top foil. In other words, a mesoscale foil bearing with a relatively large pitch and thick top foil is not as affected as its macroscale counterpart by the sagging effect. With that in mind, the sagging effect is not considered in the subsequent simulation.

### **Orbit Simulation**

Widely used method to predict bearing performance is to find bearing stiffness and damping coefficients as a function of rotating speed and fractional excitation frequency at given speed, and performing linear stability analyses [26-29, 32, 33]. In the linear stability analysis, excitation frequency-dependent bearing impedance is calculated at specific operating speed. As excitation frequency changes the modal damping changes. When modal damping changes its sign from positive to minus, the operating speed is considered unstable assuming external disturbance has a frequency component that renders the modal damping zero. However, as shown in [27], the linear stability analyses provide only bearing natural frequency at given operating speed and does not provide exact onset speed of instability. The author shows that only orbit method can

predict both natural frequency and onset speed of instability accurately. In this paper, stability characteristics and overall bearing performance are evaluated using orbit method to characterize the overall performance of the manufactured mesoscale foil gas bearings. In the current frame of work, cylindrical rigid body mode is simulated to investigate the critical speed and the maximum operating speed without instability using a sweep of 10,000 rpm increments for illustration. Although this resolution was chosen for simplicity, a much finer resolution can be implemented to search for instability.

The non-dimensional rotor equations of motion are given by

$$m_r C \omega^2 \frac{d^2 \varepsilon_X}{d\tau^2} = F_{bX} + F_{eX}, \quad (20)$$

$$m_r C \omega^2 \frac{d^2 \varepsilon_Y}{d\tau^2} = F_{bY} + F_{eY}, \quad (21)$$

where  $m_r$  is a rotor mass,  $F_{eX, Y}$  are external loads applied to the bearing including rotor weight, and  $F_{bX, Y}$  are dynamic bearing reaction forces integrated over the bearing surface.

In the orbit simulation, the trajectory of rotor center is found by solving Reynolds Equation, Eq.(9), and bump dynamics, Eq. (8), and rotor equation of motions, Eq. (20) & (21), simultaneously. The Reynolds equation is solved at every time step using the displacements and velocities of both rotor and top foil evaluated at previous time step. The orbit method uses 360 computational time grid for one cycle. The 5<sup>th</sup> order Adams-

Bashforth scheme [34] was used for time integration. More details on the accuracy of the chosen time step and orbit method can be found in [24, 27, 31].

### **Parametric Study**

A model was developed in C++ to determine the imbalanced response of the rotor and estimate the onset of instability. The dimensions of the bearing and rotor create geometric constraints that are used for determining the pressure profile in each time step using the Reynolds Equation. The pressure profile is used to determine the bearing reaction forces and determine the position of the rotor in each time step. The characteristics of the bearing affect the imbalanced response of the rotor and may be modified in the simulation to gain a more intuitive physical understanding of gas foil bearing supported turbomachinery. In other words changing the geometry in the simulation code it is possible to identify trends for stiffness, damping, vibration, etc. Establishing accurate trends for bearing parameters is useful for improving the bearing design.

Using the orbit simulation, an estimation of the amplitudes of vibration based on the operating speed may be determined and compared with experimental data. The test rig is designed to measure the vibration amplitude versus time and using LabVIEW for data acquisition it is possible to perform a Fast Fourier Transform (FFT) to determine the major frequency components. These results may be compared with the result of the C++ program. Although, the experimental verification is outside the scope of this paper it is important to note that there is a symbiotic relationship between the experimental data and the simulation.

*Simulation Parameters and Assumptions of the Bearing Model*

It is very well-known that lightly-loaded gas bearings are very unstable. As explained earlier, the manufactured bearing has a self-generated preload (see Figure 5 (a) & (b)) when the rotor is assembled in concentric with the bearing sleeve. Each sub-bearing is 2mm long and the total bearing length is 4mm as shown in Table 2.

**Table 2 Geometry and Parameters for the Simulated Air Foil Bearing.**

<b>Parameter</b>	<b>Nominal Value</b>
Inner bearing diameter (2R)	5 mm
Bearing length (L)	4 mm
Sub-bearing length	2 mm
Nominal Clearance (C)	25 $\mu\text{m}$
Top foil thickness	75 $\mu\text{m}$
Number of bumps	9
Bump stiffness per unit area	3.01 GN/m <sup>3</sup>
Bump Pitch	1.745 mm
Bump Height	0.3204 mm
*Rotor mass per sub-bearing	0.002 kg
Loss Factor	0.15-0.25

\*Note: The total rotor mass per bearing =2\*0.002 kg=0.004 kg

For the simulations, a virtual rotor which mimics a palm-sized gas turbine generator supported by three mesoscale foil gas bearing sets is envisioned. The rotor consists of a shaft (diameter = 5mm, length = 40mm) and three inertias (compressor,

turbine, and PM motor) with diameter of 12mm, and the total mass of the virtual rotor is about 12g. For the purpose of the simulation, it is assumed that the total rotor weight is evenly distributed on the three bearings, rendering a rotor mass per bearing of 4g. The 4g corresponds to less than 2% of the bearing load capacity if an average effective pressure of 1 bar is assumed on the bearing projection area. The effective pressure of 1 bar is a conservative load capacity estimation compared to many macroscale foil gas bearings [7, 24, 29, 31, 32]. The bearings are arranged in pairs such that the moments created by the preload offset in each bearing subset are balanced. In other words, when the two sub-bearings are arranged in preloaded conditions, they equally loaded in opposite direction and the rotor weight is negligible compared to the load capacity of each sub-bearing.

### **Simulation Results**

Parametric studies were performed for the different levels of preload offset distances and loss factors. Due to the unique design feature of the elastic foundation, the true level of damping is unknown without experimental measurements. Onset speed of instability, predicted stable operating within test rig capability, and steady state orbit characteristics were investigated.

#### *Effect of Preload Offset Distance*

Three different levels of preload offset distances (12 $\mu$ m, 17 $\mu$ m, and 22 $\mu$ m) were selected for comparative studies. Low frequency vibration that increases with the operating speed occurs in the cascade plot with a 12 $\mu$ m preload offset in the range of 50-

500krpm. When the operating speed reaches about 400krpm it is predicted that the rotor will crash into the bearing. However, as the preload offset is increased from 12 $\mu$ m to 17 $\mu$ m it is observed that the low frequency vibration reduces and this vibration component is completely removed with a preload offset of 22 $\mu$ m. The operating speed of this case and the remaining case are predicted to have an operating speed of above 1000krpm. Since the test rig designed is limited to operating near 500krpm it is not of any consequence to simulate further.

The reduction in low frequency vibration as the preload increases is shown in Figure 20, Figure 21, and Figure 22 which goes from a preload offset of 12-22 $\mu$ m. For brevity, only the x-direction plots are provide but the trend is observed in both directions of motion.

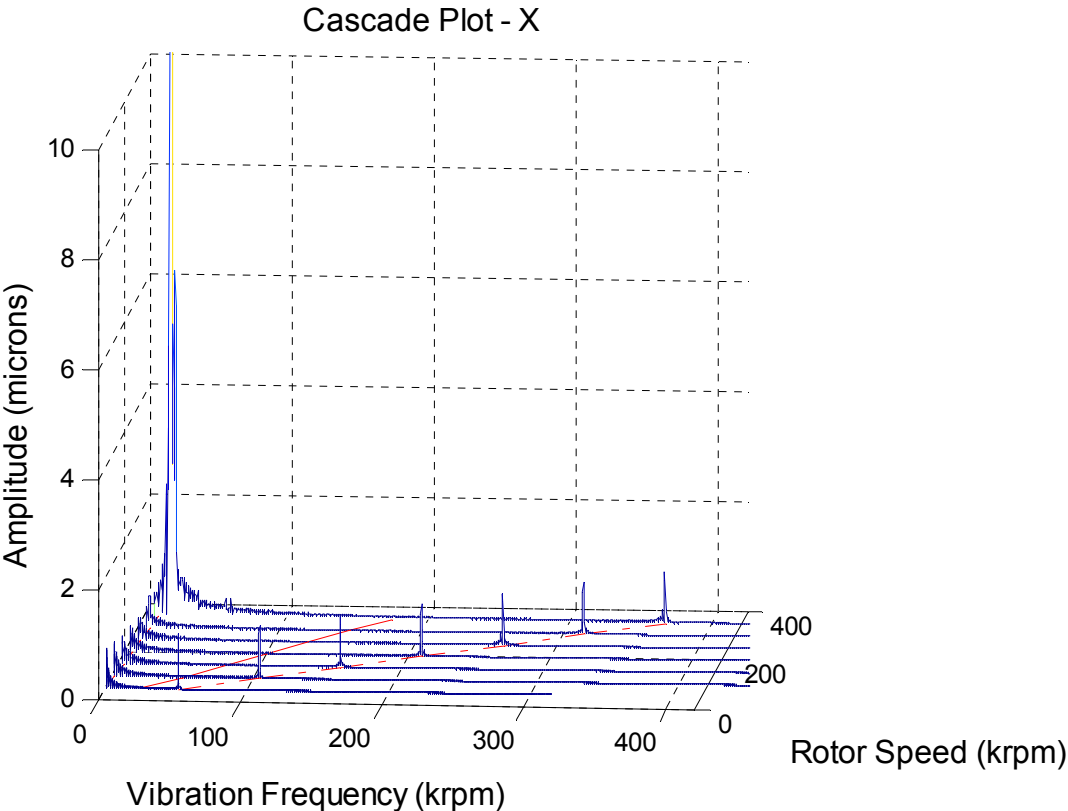
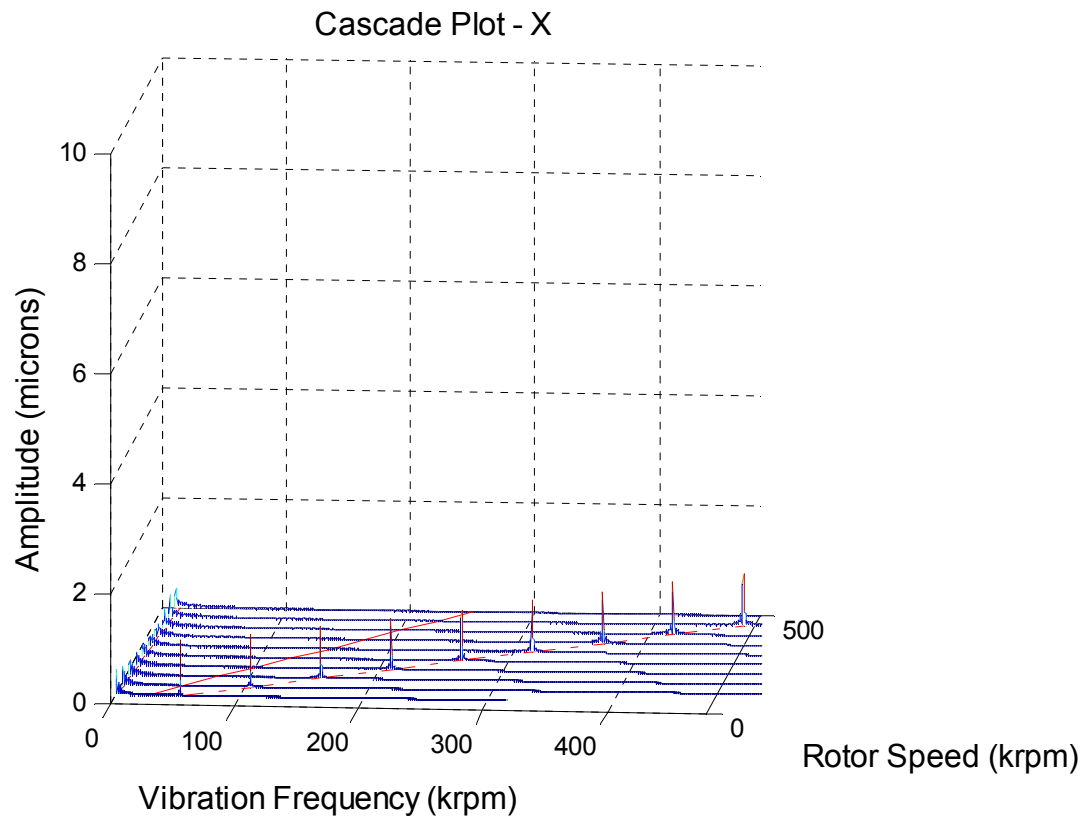
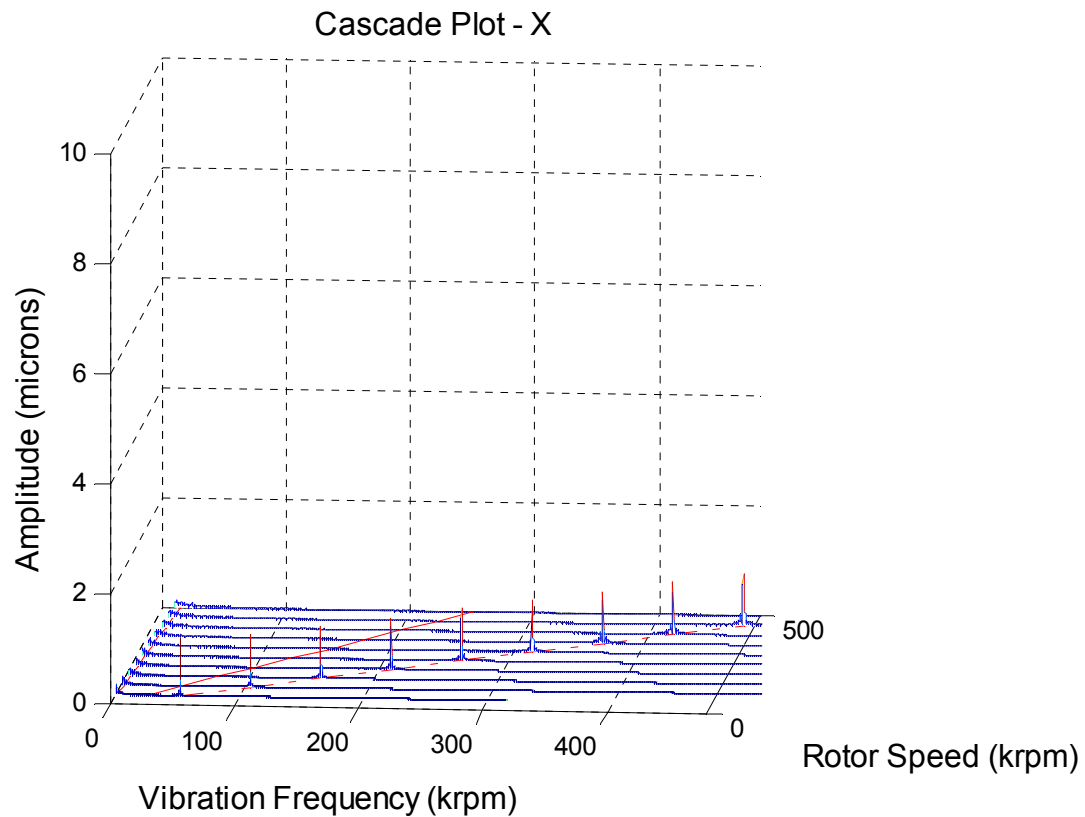


Figure 20 Cascade Plot X , 50-350krpm, PL12um, LF0.20. Preload 12um, Loss Factor 0.20, 0.03X, 0.5X, and 1.05X.



**Figure 21 Cascade Plot X, 50-500krpm, PL 17um, LF 0.20. Preload 17um, Loss Factor 0.20, 0.03X, 0.5X, and 1.05X.**



**Figure 22 Cascade Plot X, 50-500krpm, PL22um, LF 0.20. Preload 22um, Loss Factor 0.20, 0.03X, 0.5X, and 1.05X.**

### *Effect of Loss Factor*

The cascade plots for loss factors 0.15, 0.2, and 0.25 with a constant preload offset of  $17\mu\text{m}$  yielded less observable trends. The loss factor does not appear to have any effect on the vibration in the range of 50-500krpm. Comparing the three cases the small sub-synchronous vibrations are fairly constant in the x-direction (circumferential) and increase proportionally with operating speed in the z-direction (axial).

Each cascade plot where the loss factor is changed provides almost identical results in the range of 50-500krpm. All plots (Figure 21, Figure 23, and Figure 24) exhibit relatively small amplitude sub-synchronous vibration with constant synchronous components.

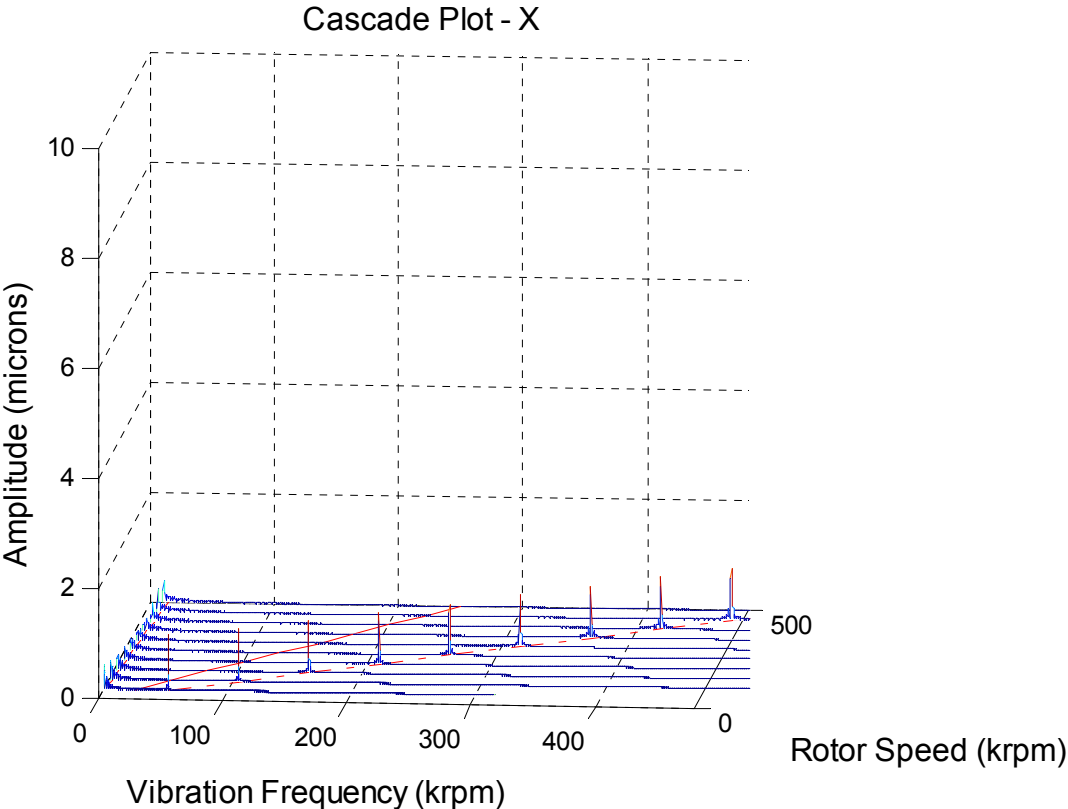


Figure 23 Cascade Plot X, 50-500krpm, PL17um, LF 0.15. Preload 17um, Loss Factor 0.15, 0.03X, 0.5X, and 1.05X.

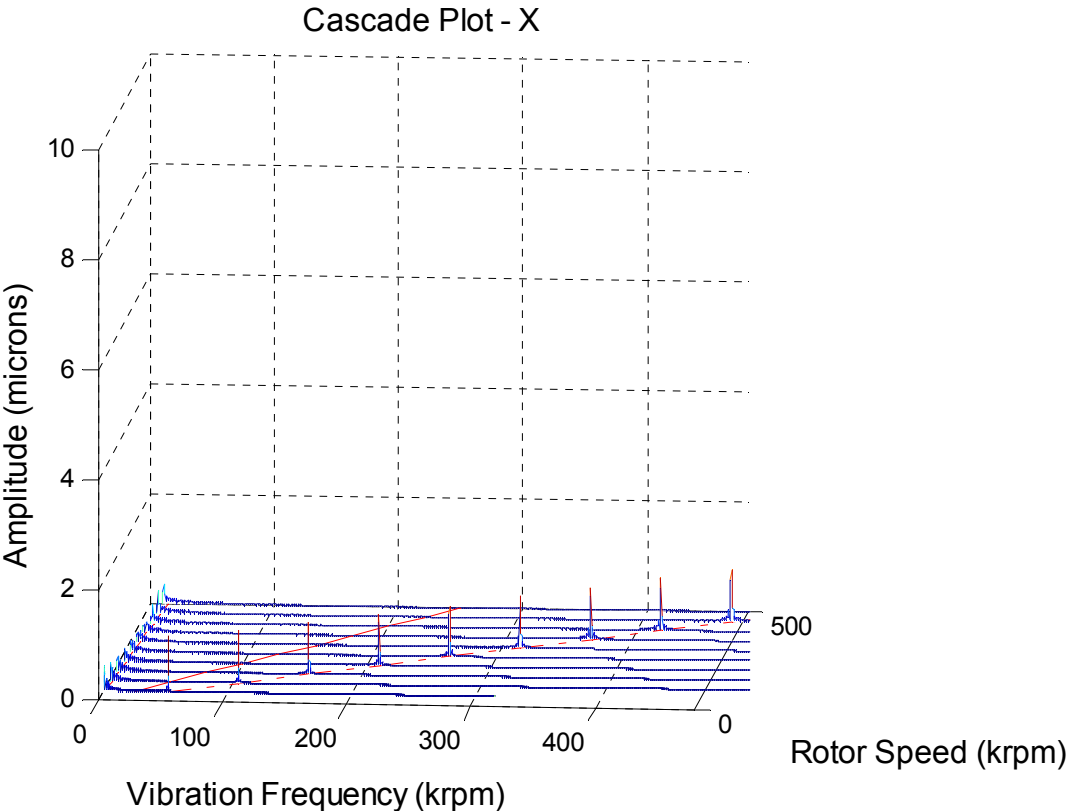


Figure 24 Cascade Plot X, 50-500krpm, PL17um, LF 0.25. Preload 17um, Loss Factor 0.25, 0.03X, 0.5X, and 1.05X.

## CHAPTER IV

### CONCLUSION AND FUTURE WORK

UV and X-ray Lithography were utilized to create a 200 $\mu$ m and 1mm elastic foundation for a gas foil bearing, respectively. A test apparatus was designed and the appropriate sensors were tested and calibrated. A comparison was made between the micro-fabrication techniques X-ray LIGA and UV-LIGA.

The predicted performance of the bearing is also investigated through the orbit simulation method and the parametric study gave insight to the preload effects on stability and the maximum operating speed. The unique features of the gas foil bearing introduced provide great promise in terms of its application considering the high stable operating speed just below 4110 krpm in select cases.

It has been established in a previous study [27] that the major difference in dynamic stability as a result of bearing performance comes from the overall bearing shape. It was stated that the force coefficients are weak functions of stiffness variations. This is due to the fact that stiffness variation along either the axial or circumferential direction does not have as strong an impact on the load capacities and overall force coefficients as does the overall bearing shape. Therefore, it stands to reason that given the large sweeping increment used to vary the operating speed for the parametric study a small effect could be outside the resolution of the search in this study.

Furthermore to complete the first overall design of the gas foil bearing, experimental results are absolutely necessary. A comparison of the simulation and the

experimental results from the test rig designed in this research could clarify trends for important bearing parameters. With this type of information the simulation can be made less idealized and also more robust. Great understanding was gained in terms of the preload offset and stability, however increasing the resolution of the stability sweep and obtaining comparable experimental results are crucial to thoroughly understand the bearing designed.

## REFERENCES

- [1] Agrawal, G. L., 1997, "Foil Air/Gas Bearing Technology—An Overview," ASME Paper No. 97-GT-347.
- [2] Heshmat, H., Walowit, J. A., and Pinkus, O., 1983, "Analysis of Gas-Lubricated Foil Journal Bearings," *Journal of Lubrication Technology-Transactions of the ASME*, **105**(4), pp. 647-655.
- [3] Agrawal, G. L., 1998, "Foil Air Bearings Cleared to Land," *Mechanical Engineering*, **120**(7), pp. 78-80.
- [4] Ku, C. P. R., Heshmat, H., 1992, "Compliant Foil Structural Stiffness Analysis, Part I: Theoretical Model," *ASME Journal of Tribology*, **114**(2), pp. 394-400.
- [5] Ku, C. P. R., Heshmat, H., 1992, "Compliant Foil Structural Stiffness Analysis, Part II: Experimental Investigation," *ASME Journal of Tribology*, **115**(3), pp. 364-369.
- [6] Peng, J.P., and Carpino, M., 1992, "Calculation to Stiffness and Damping Coefficients for Elastically Supported Gas Foil Bearings," *ASME Journal of Tribology*, **115**, pp. 20-27.
- [7] Heshmat, H., 1994, "Advancements in the Performance of Aerodynamic Foil Journal Bearings - High-Speed and Load Capability," *Journal of Tribology-Transactions of the ASME*, **116**(2), pp. 287-295.
- [8] Carpino, M., 1997, "Finite Element Approach to the Prediction of Foil Bearing Rotor Dynamic Coefficients," *ASME Journal of Tribology*, **119**, pp. 85-90.
- [9] Vleugels, P., Waumans, T., Peirs, J., Al-Bender, F., and Reynaerts, D., 2006, "High-Speed Bearings for Micro Gas Turbines: Stability Analysis of Foil Bearings," *Journal of Micromechanics and Microengineering*, **16**(9), pp. S282-S289.
- [10] Yongbok Lee, K. R., and Chang-Ho Kim, 2004, "Preliminary Test Results of Rotordynamic Characteristics for 100 Watts Class Micro Power System," *Technical Digest PowerMEMS*, pp. 179-182.
- [11] Vleugels, P., Waumans, T., Peirs, J., Al Bender, F., and Reynaerts, D., 2006, "High-Speed Foil Bearings for Micro Gas Turbines: Stability Analysis of Foil Bearings," *Journal of Micromechanics and Microengineering*, **16**, pp. S282-S289.
- [12] Dellacorte, C., 2008, "Oil-Free Turbomachinery Program," <http://www.grc.nasa.gov/WWW/Oilfree/bearings.htm>
- [13] Sim, K., and Kim, D., 2007, "Design of Flexure Pivot Tilting Pads Gas Bearings for High-Speed Oil-Free Micro Turbomachinery," *ASME Journal of Tribology*, **129**(1), pp. 112-119.
- [14] Ehrfeld, W., Hessel, V., Lowe, H., Schilz, C., and Weber, L., 1999, "Materials of LIGA Technology," *Springer Microsystem Technologies*, **5**, pp. 105–112.

- [15] Liu, J., Cai, B., Zhu, J., Ding, G., Zhao, X., Yang, C., and Chen, D., 2004, "Process Research of High Aspect Ratio Microstructure Using Su-8 Resist," *Microsystem Technologies-Micro-and Nanosystems-Information Storage and Processing Systems*, **10**(4), pp. 265-268.
- [16] Lawes, R. A., 2005, "Manufacturing Tolerances for UV LIGA Using Su-8 Resist," *Journal of Micromechanics and Microengineering*, **15**(11), pp. 2198-2203.
- [17] Thian, S., Tang, Y., Fuh, J. Y. H., Wong, Y. S., Loh, H. T., Lu, L., and Tee, D. Z. S., 2006, "Formation of Micromoulds Via Uv Lithography of Su8 Photoresist and Nickel Electrodeposition," *Proceedings of the Institution of Mechanical Engineers Part B-Journal of Engineering Manufacture*, **220**(2), pp. 329-333.
- [18] Kim, D., 2004, "Design and Fabrication of Sub-Millimeter Scale Gas Bearings with Tungsten-Containing Diamond Like Carbon Coatings," Ph.D. thesis, University of Texas at Austin, Austin, TX.
- [19] Di Bari, G. A., 1994, *Nickel Plating, Surface Engineering, ASM Handbook*, ASM International, Materials Park, OH.
- [20] Parthasaradhy, N. V., 1989, *Practical Electroplating Handbook*, Prentice Hall, Upper Saddle River, NJ.
- [21] Seet, K. K., Mizeikis, V., Juodkazis, S., and Misawa, H., 2006, "Spiral Three-Dimensional Photonic Crystals for Telecommunications Spectral Range," *Applied Physics a-Materials Science & Processing*, **82**(4), pp. 683-688.
- [22] Sameoto, D., Tsang, S. H., Foulds, I. G., Lee, S. W., and Parameswaran, M., 2007, "Control of the out-of-Plane Curvature in Su-8 Compliant Microstructures by Exposure Dose and Baking Times," *Journal of Micromechanics and Microengineering*, **17**(5), pp. 1093-1098.
- [23] Timoshenko, S. P., and Goodier, J. N., 1970, *Theory of Elasticity*, McGraw-Hill, New York.
- [24] Song, J. H., and Kim, D., 2007, "Foil Gas Bearing with Compression Springs: Analyses and Experiments," *Journal of Tribology-Transactions of the ASME*, **129**(3), pp. 628-639.
- [25] Rubio, D., and San Andrés, L., 2005, "Structural Stiffness, Dry-Friction Coefficient and Equivalent Viscous Damping in a Bump-Type Foil Gas Bearing," Technical Report No. GT 2005-68384, ASME.
- [26] Peng, J.-P., and Carpino, M., 1993, "Calculation to Stiffness and Damping Coefficients for Elastically Supported Gas Foil Bearings," *ASME Journal of Tribology*, **115**, pp. 20-27.
- [27] Kim, D., 2007, "Parametric Studies on Static and Dynamic Performance of Air Foil Bearings with Different Top Foil Geometries and Bump Stiffness Distributions," *Journal of Tribology-Transactions of the ASME*, **129**(2), pp. 354-364.

- [28] Carpino, M., and Talmage, G., 2006, "Prediction of Rotor Dynamic Coefficients in Gas Lubricated Foil Journal Bearings with Corrugated Sub-Foils," *Tribology Transactions*, **49**(3), pp. 400-409.
- [29] Carpino, M., and Talmage, G., 2003, "A Fully Coupled Finite Element Formulation for Elastically Supported Foil Journal Bearings," *Tribology Transactions*, **46**(4), pp. 560-565.
- [30] Hamrock, B. J., Jacobson, B. O., and Schmid, S. R., 2004, *Fundamentals of Fluid Film Lubrication*, Marcel Dekker Inc, New York, NY.
- [31] Kim, D., and Park, S., 2007, "Hybrid Air Foil Bearings with External Pressurization," Accepted to *ASME Journal of Tribology*.
- [32] Kim, T. H., and Andres, L. S., 2008, "Heavily Loaded Gas Foil Bearings: A Model Anchored to Test Data," *Journal of Engineering for Gas Turbines and Power-Transactions of the ASME*, **130**(1), pp. 012504-1-8.
- [33] San Andrés, L., and Kim, T. H., 2006, "Computational Analysis of Gas Foil Bearings Integrating 1d and 2d Finite Element Models for Top Foil," Technical Report No. B&C-1-06, Turbomachinery Laboratory, Texas A&M University, College Station, TX.
- [34] Chapra, S. C., and Canale, R. P., 1989, *Numerical Methods for Engineers*, McGraw-Hill, New York, NY.

## APPENDIX A

The following table provides the original data from the substrate processing.

**Table 3 Original Data from UV-Lithography.**

Date	Wafer Type	Cr thickness (nm)	Au thickness (nm)	Goal Thickness (microns)	SU-8 Type	Primer	Base Resistance (Ohms)	Primer Spin Speed	Primer bake time (min)	Primer Bake Temp (deg C)	Resist Spin Speed (rpm)
3/3/2007	Si			200	2075	none					1340-1350
4/8/2007	Si			200	2075						1330-1340
4/14/2007	Si			50	2050						1282-1290
4/11/2007	Si			50	2050						2029-2039
4/15/2007	Si			500	2150						1218-1219
4/18/2007	Si			500	2150						1110
4/20/2007	Si			500	2150						1108-1118
4/23/2007				500	2150						1126-1131
5/12/2007	Si			200	2075						1288-1304
5/18/2007	Si			500	2150						1107-1120
5/18/2007	Si/ Cr/ Au	50	50	500	2150						1110-1126
5/4/2007	Si/ Cr	60		500	2150						1095-1104
5/21/2007	Si/ Cr/ Au	50	50	500	2150						1092-1107
5/21/2007	Si/ Cr/ Au	50	50	500	2150	HMD S					1084-1107
6/11/2007	Si/ Cr/ Au	50	50	200	2075	Omni Coat		3091- 3101	1:30	200	1325-1336

Table 3 Continued.

Date	Wafer Type	Cr thickness (nm)	Au Thickness (nm)	Goal Thickness (micron)	SU-8 Type	Primer	Base Resistance (Ohms)	Primer Spin Speed	Primer bake time (min)	Primer Bake Temp (deg C)	Resist Spin Speed (rpm)
6/11/2007	Si/Cr/Au			200	2075						
6/15/2007	Si/Cr/Au	51	51.5	200	2075	Omni Coat		3018-3028			1327-1338
6/15/2007 A	Si/Cr/Au	51	51.5	200	2075	Omni Coat		3018-3028			1328-1340
6/17/2007 B	Si/Cr/Au	50	50	200	2075	Omni Coat	6.9-8.1	3007-3019	1:00	200	1326-1338
6/29/2007 A	Si/Cr/Au	50.2	37.3	200	2075	HMDS	10.5-12.5	3017-3024	2:01	200	1270-1298
6/29/2007 B	Si/Cr/Au	50.2	37.3	200	2075	HMDS	8.4-10.8	3020-3028	2:01	200	1290-1304
7/14/2007 A	Si/Cr/Au	50.3	51.1	500	2150	Omni Coat	On wafer Check it	1021-1036	2:02	120	1084-1097
7/14/2007 B	Si/Cr/Au	50.3	51.1	500	2150	Omni Coat	On wafer Check it	1035-1052	2:01	120	1090-1106
7/16/2007 A	Si/Cr/Au	50.3	51.1	500	2150	Omni Coat	8.6-10.6	1005-1027	2:02	120	1062-1074
7/16/2007 B	Si/Cr/Au	50.3	51.1	500	2150	Omni Coat	8.0-8.4	977-993	2:04	120	1048-1057
7/23/2007 A	Si/Cr/Au	50.8	50.4	500	2150	Omni Coat	8.8-10.0	924-945	2:01	120	983-1003
7/23/2007 B	Si/Cr/Au	50.8	50.4	500	2150	Omni Coat	9.3-8.6	965-985	2:18	120	965-985
3/3/2007	7:00			30.0	5:00	12:21	17:20				
4/8/2007	2:00	30:15			2:00	17:15					
4/14/2007	9:20	109:08		60.0							
4/11/2007	2:15	20:20		18.0	1:12		6:05				
4/15/2007	15:05 @20 deg.	130:04		45.0	5:00	28:08					
4/18/2007	8:50	109:20		46.4							
4/20/2007	15:10	126:15		46.4	5:00	28:08	34:00				
4/23/2007	16:00	125:00		46.4	15:00	125:00	32:08				

Table 3 Continued.

Date	Soft bake Time @ 65 (min)	Soft bake Time @ 95 (min)	Cool Down Time (hrs)	Exposure Time (sec)	PEB @ 65 (min)	PEB @ 95 (min)	SU-8 Development Time (min)	Primer Development	Final Resistance (ohms)
5/12/2007	7:15	39:25		26.3	5:00	16:00	25:49		
5/18/2007	15:00	125:00		44.9	5:00	28:00	40:00		
5/18/2007	15:00	125:00		67.3	5:00	28:00	40:00		
5/4/2007	15:00	225:00		69.6	5:00	28:00	50:00		
5/21/2007	11:00	125:34		46.4	6:34	28:08	44:00		
5/21/2007	11:00	125:34		46.4	6:34	28:08	44:00		
6/11/2007	7:35	41:15		26.3	6:01	16:15	21:08		
6/11/2007	7:35	41:15		26.3	5:08	16:25	21:08		
6/15/2007	7:25	41:33		39.4	6:00	16:14	26:34		7.9
6/15/2007 A	7:25	41:53		26.3	6:00	16:14	26:04		7.4
6/17/2007 B	7:14	39:14		39.4	7:14	39:35	31:24	RIE	6.8-7.3
6/29/2007 A	7:00	16:20	2	35.4	6:12	17:11	25:33	RIE	
6/29/2007 B	7:00	16:20	2	31.5	6:12	17:11	25:33:00	RIE	
7/14/2007 A	17:00	126:00	12	44.0	15:00	Left over night			
7/14/2007 B	16:00	126:00	12	41.8	15:00	Left over night			
7/16/2007 A	16:44	141:30	2	41.7	16:20	29:00	32:00	RIE	7.6-8.8
7/16/2007 B	16:44	141:30	2	46.4	16:20	29:00	32:00	RIE	7.3-7.7
7/23/2007 A	16:05	150:00	2	46.4	5:10	32:00	32:00	RIE	
7/23/2007 B	16:05	150:00	2	46.4	5:10	32:00	35:00	RIE	

## APPENDIX B

*Measurement Calibration, Fiber Optic Sensor Position Measurement Calibration*

Power Supply: BK Precision DC Regulated Power Supply 1627A

**Table 4 Initial Conditions Data Fiber Optic Sensor (FOS) 2618.**

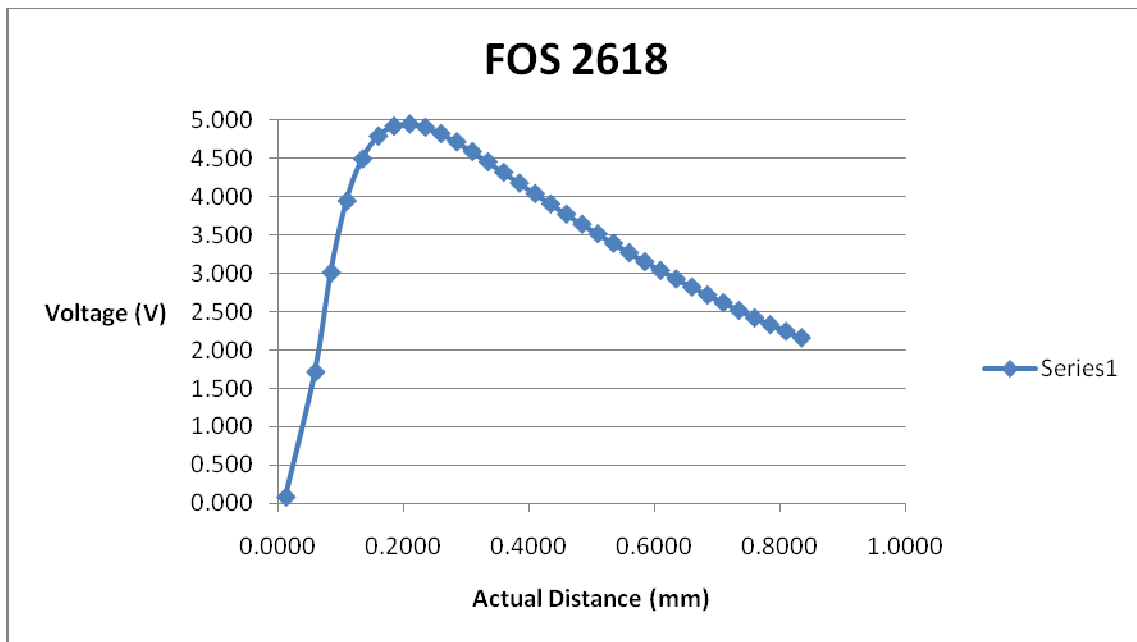
Initial Gap (mm)	Voltage (V)	Current (A)	Calibration Voltage (V)
0.0127	12.0	0.08	5.001

**Table 5 Original Measurement Data Fiber Optic Sensor (FOS) 2618.**

Voltage (V)	Actual Gap (mm)	Micrometer Gap (mm)
0.083	0.0127	6.428
1.711	0.0597	6.475
3.008	0.0847	6.500
3.941	0.1097	6.525
4.488	0.1347	6.550
4.786	0.1597	6.575
4.915	0.1847	6.600
4.943	0.2097	6.625
4.902	0.2347	6.650
4.818	0.2597	6.675
4.711	0.2847	6.700
4.586	0.3097	6.725
4.451	0.3347	6.750
4.314	0.3597	6.775
4.174	0.3847	6.800
4.037	0.4097	6.825
3.902	0.4347	6.850
3.769	0.4597	6.875
3.638	0.4847	6.900
3.513	0.5097	6.925
3.389	0.5347	6.950
3.266	0.5597	6.975
3.148	0.5847	7.000
3.035	0.6097	7.025
2.924	0.6347	7.050
2.819	0.6597	7.075
2.715	0.6847	7.100

**Table 5 Continued.**

Voltage (V)	Actual Gap (mm)	Micrometer Gap (mm)
2.615	0.7097	7.125
2.515	0.7347	7.150
2.418	0.7597	7.175
2.329	0.7847	7.200
2.242	0.8097	7.225
2.158	0.8347	7.250

**Figure 25 Fiber Optic Sensor 2618. Voltage vs Distance Response.**

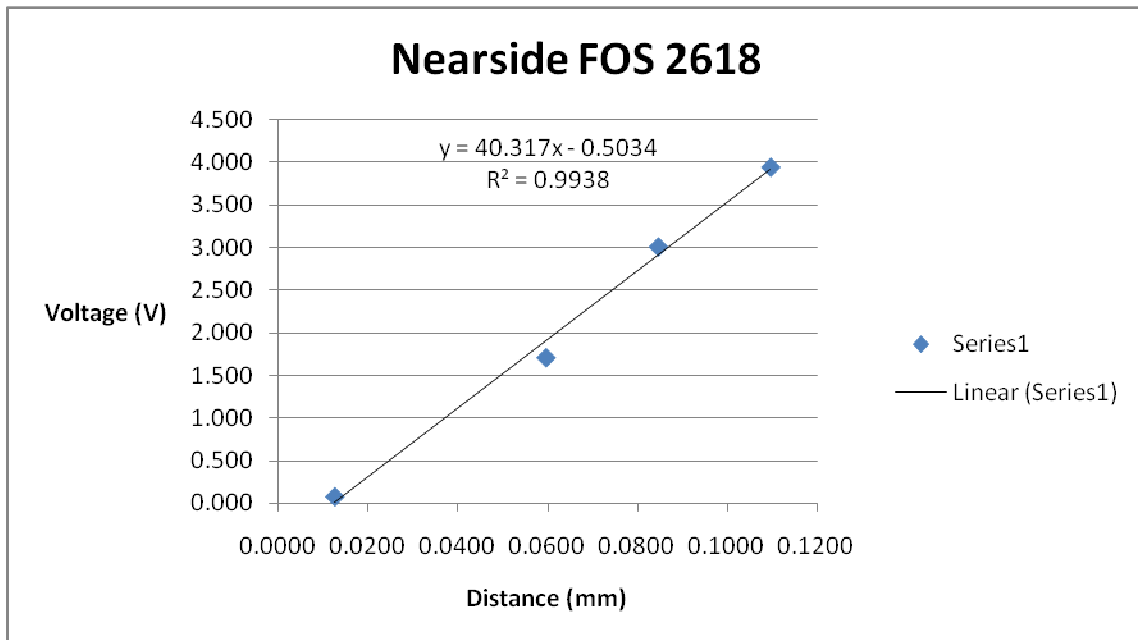


**Figure 26 Fiber Optic Sensor 2618: First Linear Region. Voltage vs Distance Response Calibration Curve.**

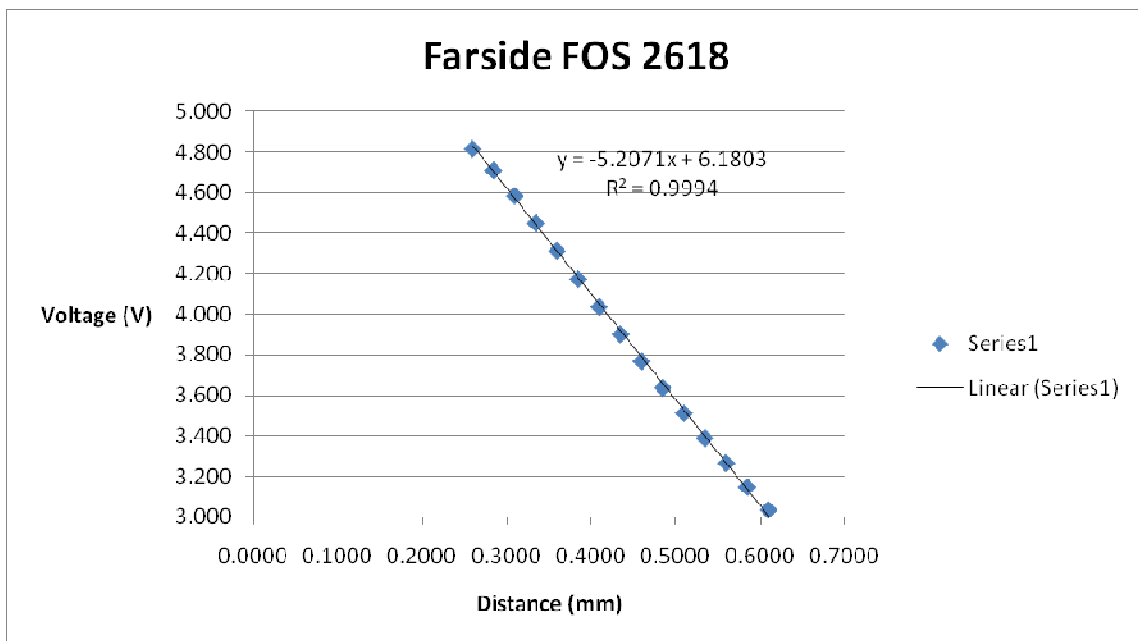


**Figure 27 Fiber Optic Sensor 2618: Second Linear Region. Voltage vs Distance Response Calibration Curve.**

**Table 6 Initial Conditions Data Fiber Optic Sensor (FOS) 2619.**

Initial Gap (mm)	Voltage (V)	Current (A)	Calibration Voltage (V)
0.0127	12.0	0.08	4.999

**Table 7 Original Measurement Data Fiber Optic Sensor (FOS) 2619.**

Voltage (V)	Actual Gap (mm)	Micrometer Gap (mm)
0.289	0.0127	6.350
1.785	0.0377	6.375
3.324	0.0627	6.400
4.266	0.0877	6.425
4.734	0.1127	6.450
4.924	0.1377	6.475
4.975	0.1627	6.500
4.941	0.1877	6.525
4.862	0.2127	6.550
4.759	0.2377	6.575
4.646	0.2627	6.600
4.519	0.2877	6.625
4.380	0.3127	6.650
4.238	0.3377	6.675
4.099	0.3627	6.700
3.956	0.3877	6.725
3.815	0.4127	6.750
3.677	0.4377	6.775
3.546	0.4627	6.800
3.418	0.4877	6.825
3.292	0.5127	6.850
3.171	0.5377	6.875
3.055	0.5627	6.900
2.940	0.5877	6.925
2.835	0.6127	6.950
2.731	0.6377	6.975
2.630	0.6627	7.000
2.532	0.6877	7.025
2.440	0.7127	7.050
2.350	0.7377	7.075
2.262	0.7627	7.100
2.181	0.7877	7.125
2.098	0.8127	7.150

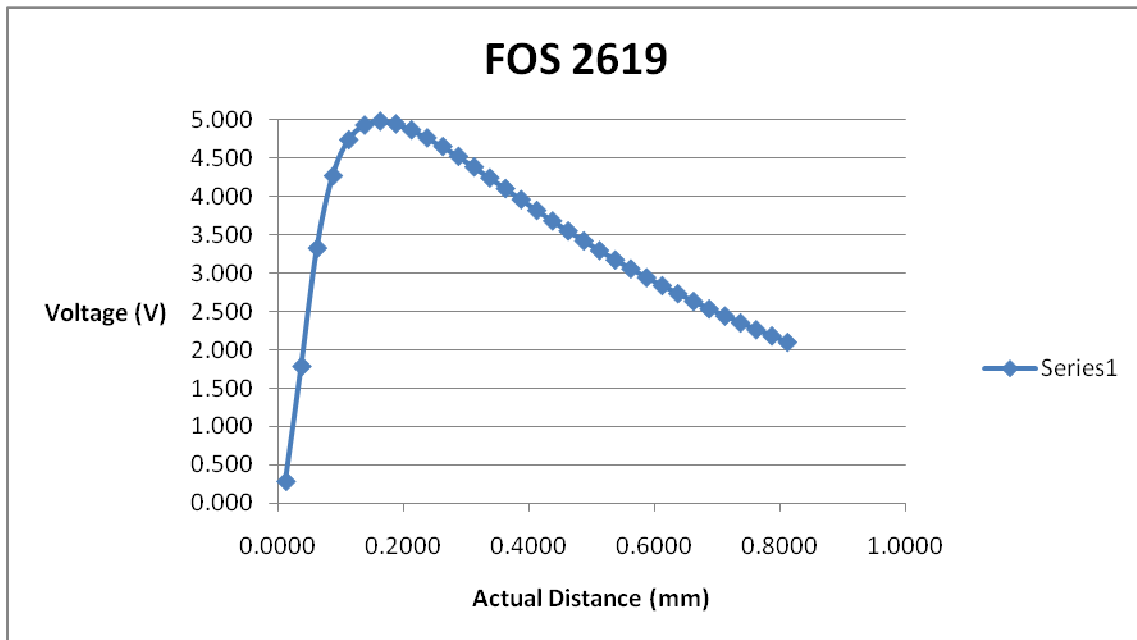


Figure 28 Fiber Optic Sensor 2619. Voltage vs Distance Response.

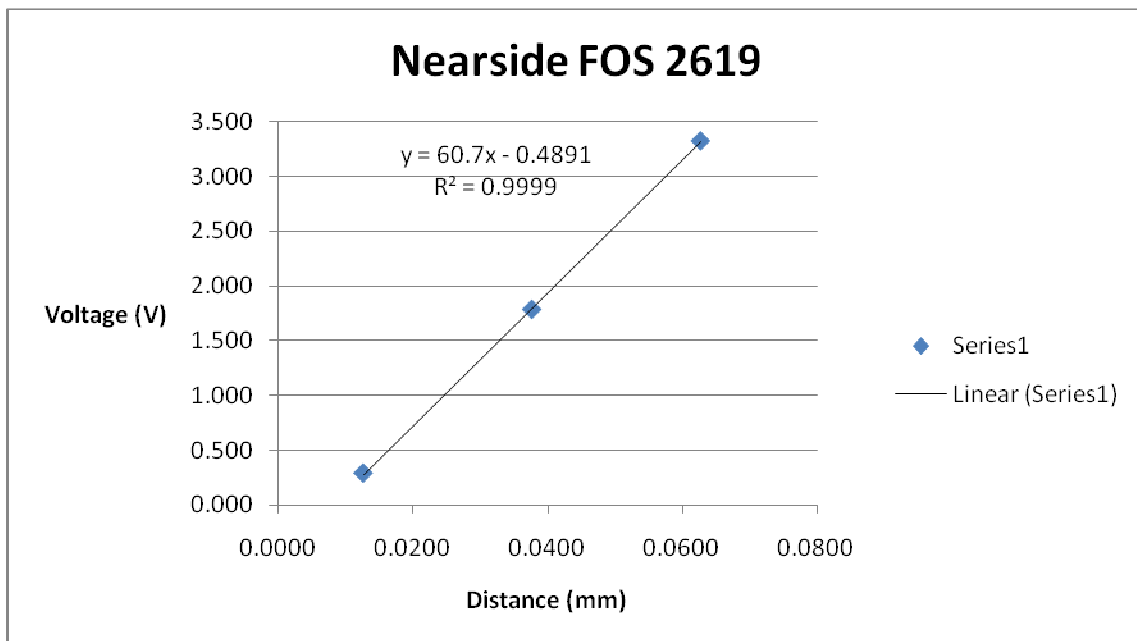
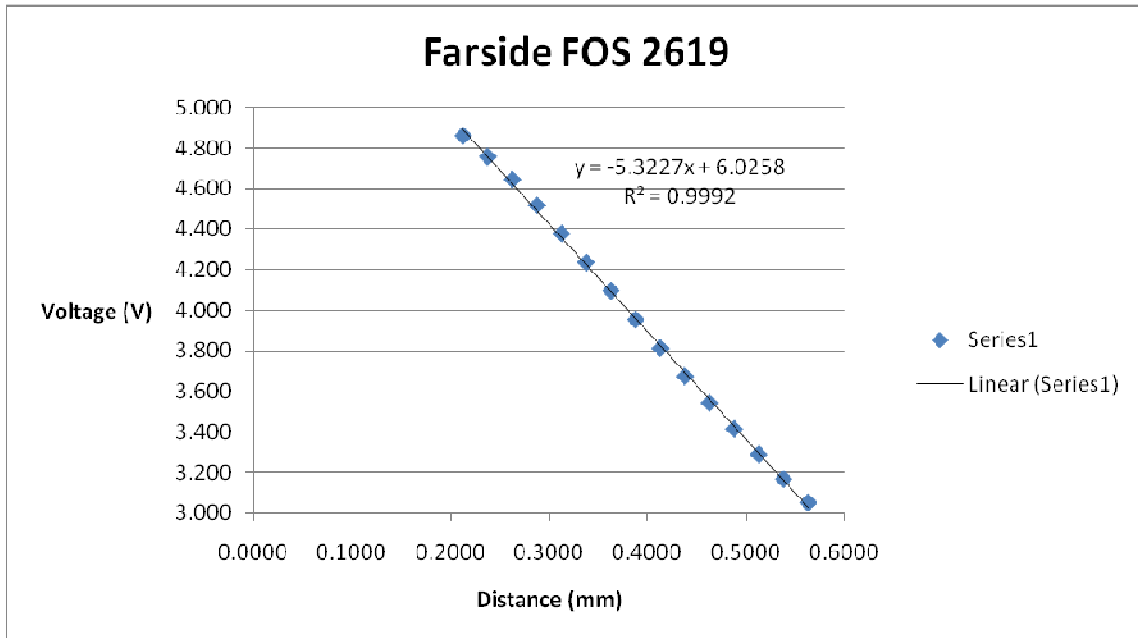


Figure 29 Fiber Optic Sensor 2619: First Linear Region. Voltage vs Distance Response.



**Figure 30 Fiber Optic Sensor 2618: Second Linear Region. Voltage vs Distance Response.**

## APPENDIX C

*SEM Analysis*

The scanning electron microscope was used at different stages of the micro-fabrication processing to check the quality of the pattern transfer. It is observed that the polymer is removed mostly but there are some areas in which SU-8 remained after the removal process. This is one the disadvantageous associated with a strong novolac resin. Recently, many chemists have developed photoresists that incorporate the advantages of SU-8 without the removal problem observed in these SEM images. However, SU-8 and PMMA were the only photoresists used in the project but it is an obvious area of the bearing design that must be improved.

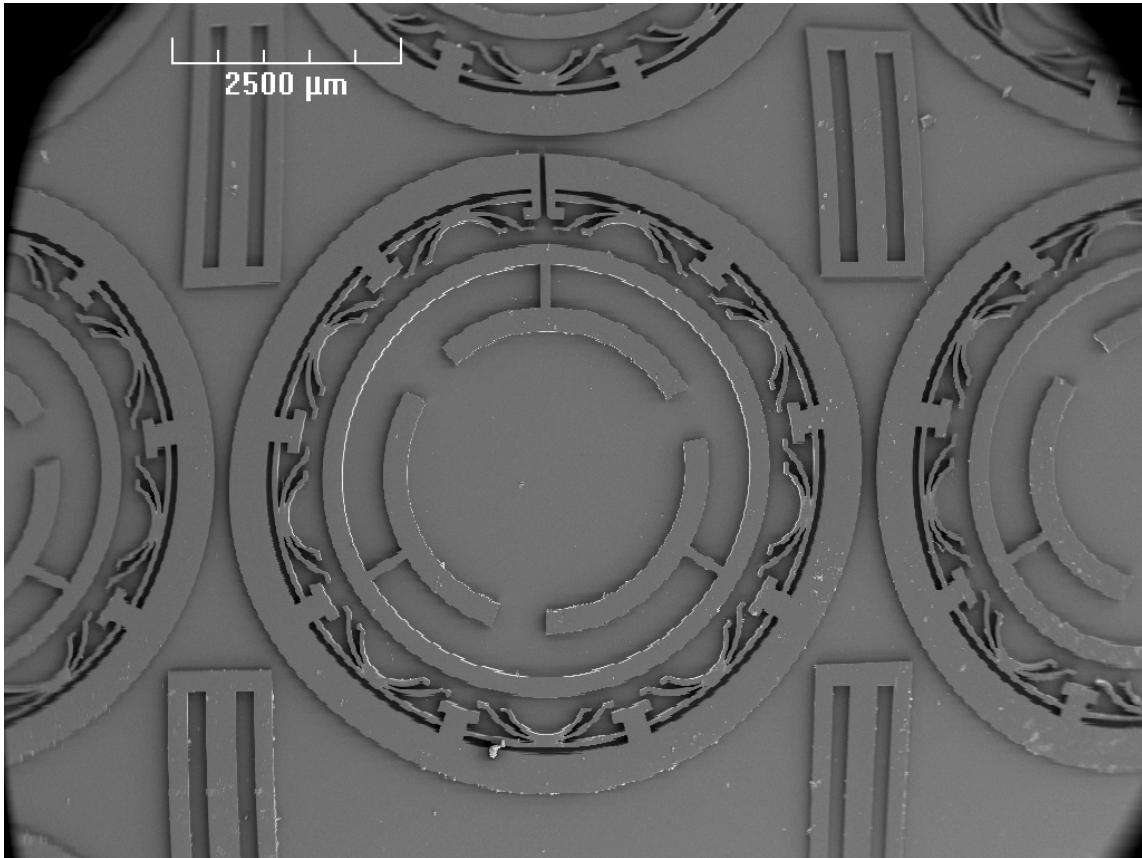


**Figure 31 SU-8 Pattern. Elastic Foundation for Foil Bearing, Magnification 15X, 20eV.**

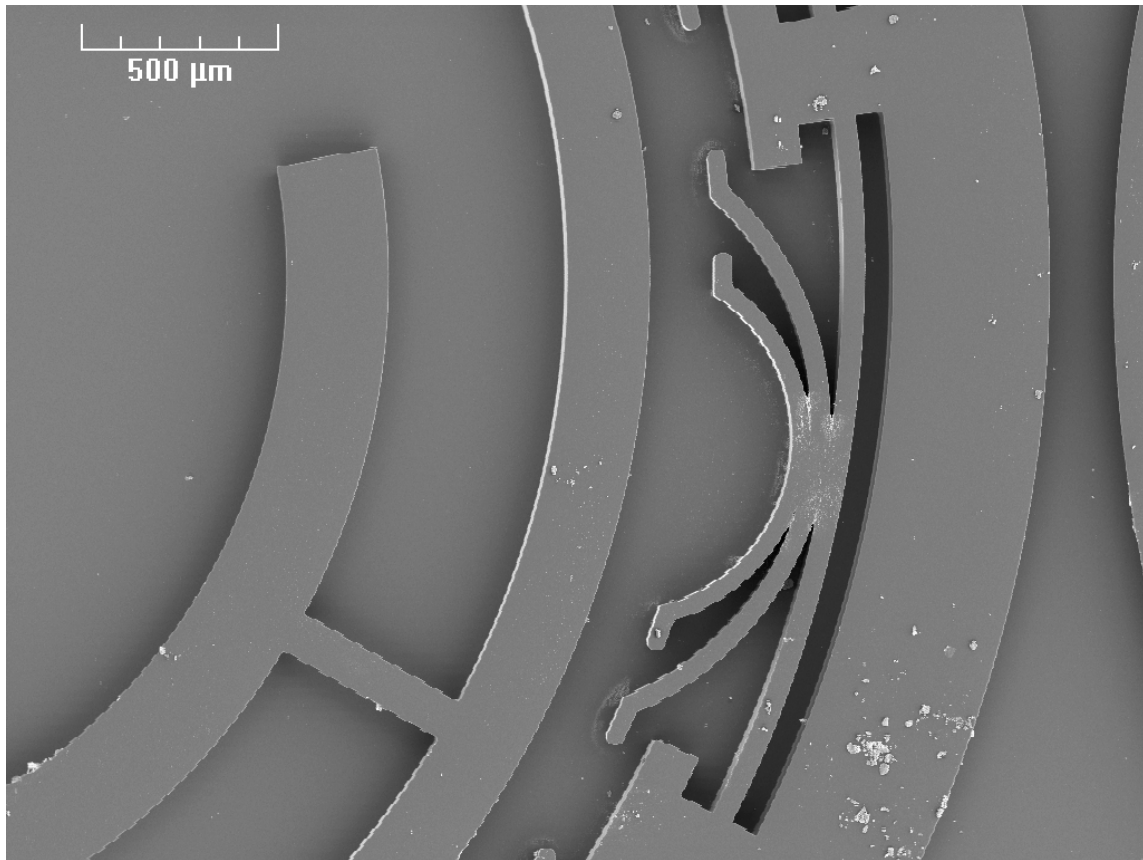


**Figure 32 Detail of the SU-8 Pattern. Elastic Foundation for Foil Bearing, Magnification 50X, 20eV.**

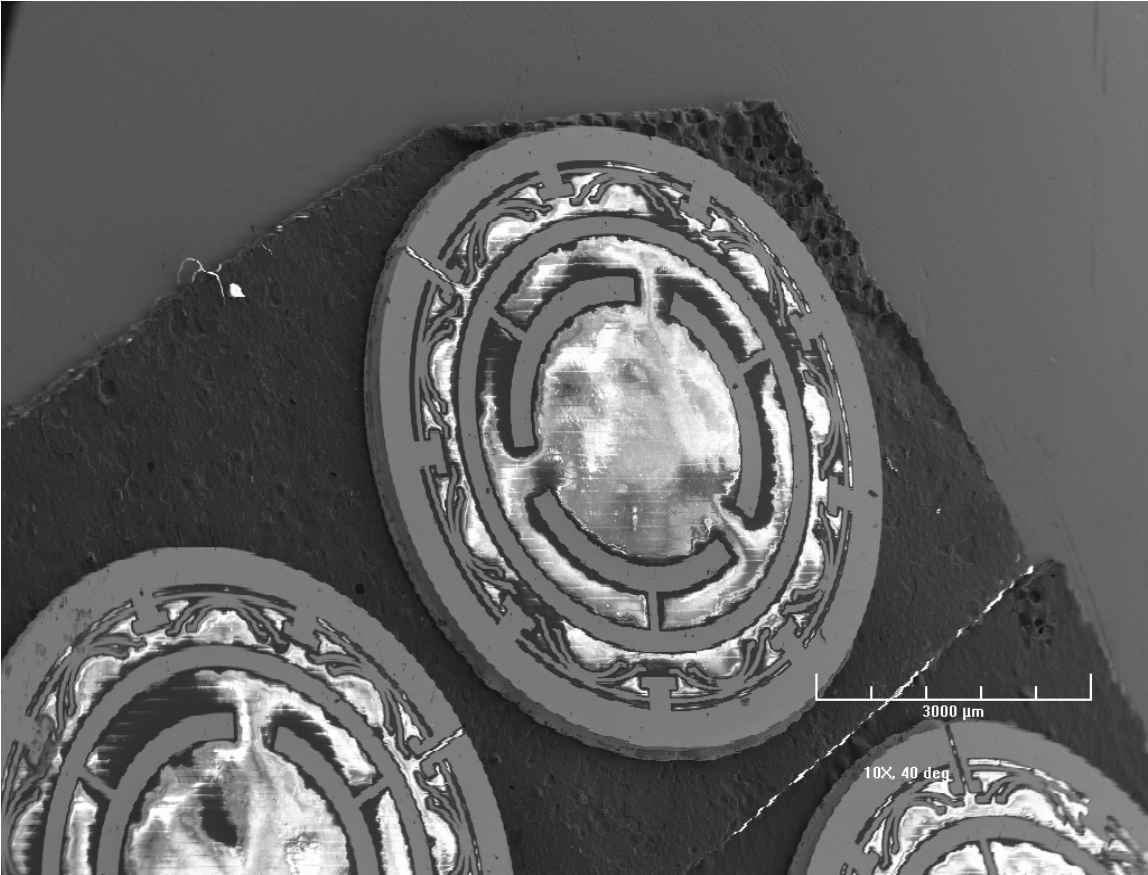


**Figure 33 Multiple Electroplated Elastic Foundations for Foil Bearing. Magnification 10X and 20eV, Angle 40 deg.**

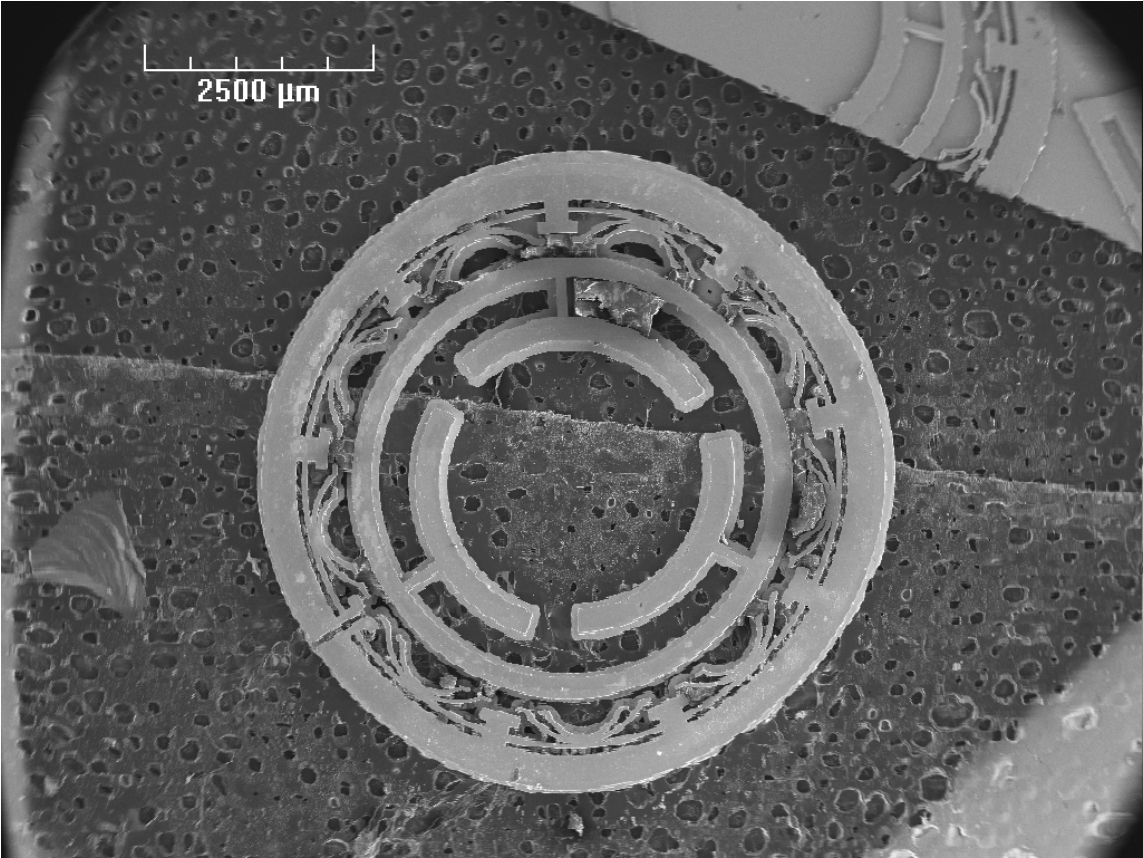


**Figure 34 Single Electroplated Elastic Foundation for Foil Bearing. Magnification 15X and 20eV.**

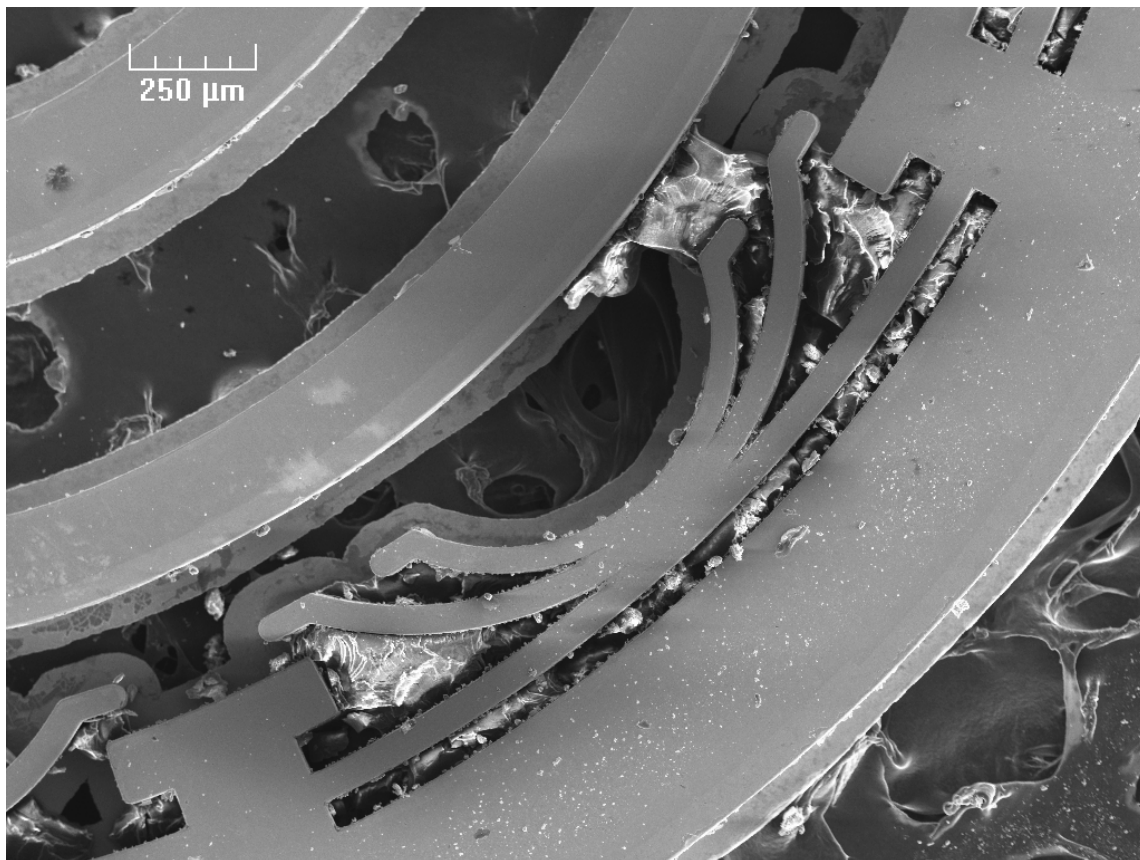


**Figure 35** Detail of the Single Electroplated Elastic Foundation. Foil Bearing, Magnification 50X, 20eV.

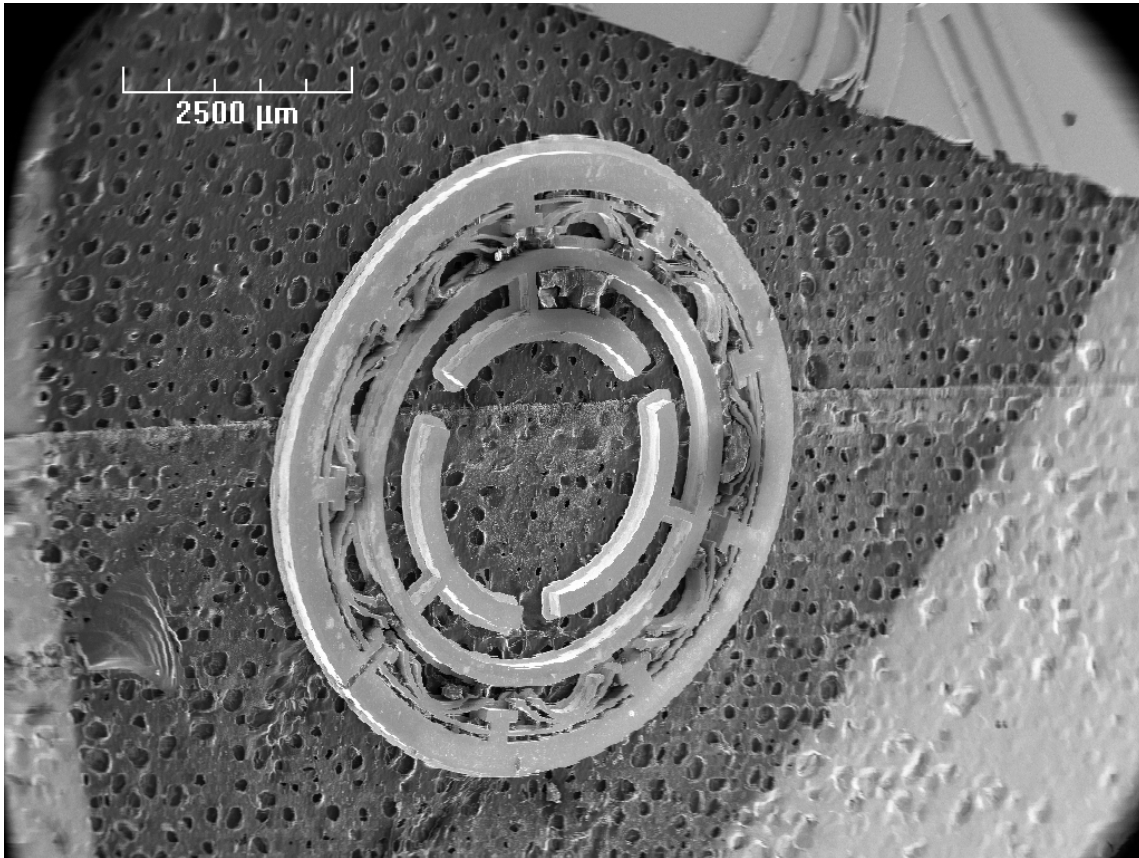


**Figure 36 Electroplated Elastic Foundation for Foil Bearing. Magnification 10X, 20eV, Angle 25 deg.**

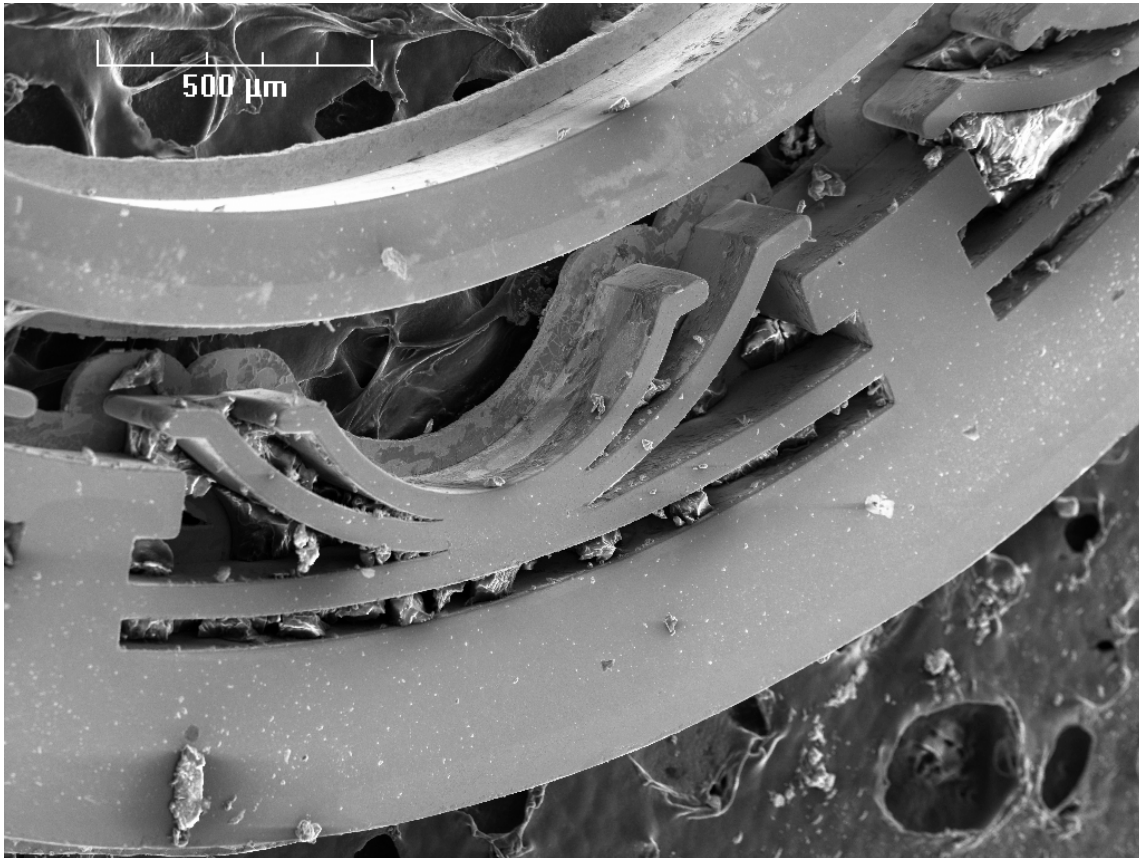


**Figure 37** Detail of the Electroplated Elastic Foundation for Foil Bearing. Magnification 15X, 20eV, Angle 25 deg.

## VITA

Name: Andron Jaykondor Creary

Address: Texas A&M University,  
Department of Mechanical Engineering,  
3123 TAMU,  
College Station, TX 77843-3123

Email Address: andron4@gmail.com

Education: B.S., Mechanical Engineering, Florida State University, 2006  
M.S., Mechanical Engineering, Texas A&M University, 2009

Publications: Kim, D., Creary, A., Chang S., Kim J. , 2008. "Meso-Scale Foil Gas Bearings for Palm-Sized Turbomachinery: Design, Manufacturing, and Modeling," Accepted to ASME Journal of Engineering for Gas Turbines and Power.

Conference Presentations:

Creary, A. , "Mesoscale Airfoil Bearings for 100~200W Class Micro Power Generation," National Science Foundation Joint Annual Meeting, Washington D.C., August 2007.

Creary, A. , Lui, L., and Qian, L., "Control Demonstration Using Virtual Test Bed," Electric Ship Research and Development Consortium, University of South Carolina, May 31- June 1 2006, <http://vtb.ee.sc.edu/review/ESRDCMayMeeting/PosterSession2.htm>.

Honors and Awards:

Louis Stokes Alliance for Minority Participation (National Science Foundation) Fellowship	Aug. 2006 – July 2008
--	-----------------------

Texas A&M Department of Mechanical Engineering First Year Graduate Student Fellowship	Aug. 2006 – May 2007
--	----------------------

Crawford Fellowship	Aug. 2006 – May 2007
---------------------	----------------------

Florida Bright Futures Scholarship	Jun. 2000 – May 2006
------------------------------------	----------------------